

# A channel selection methodology for enhancing volcanic SO<sub>2</sub> monitoring using FY-3E/HIRAS-II hyperspectral data

Xinyu Li<sup>2</sup>, Lin Zhu<sup>1</sup>, Hongfu Sun<sup>2</sup>, Jun Li<sup>1</sup>, Ximing Lv<sup>2</sup>, Chengli Qi<sup>1</sup>, Huanhuan Yan<sup>1</sup>

<sup>1</sup> Key Laboratory of Radiometric Calibration and Validation for Environmental Satellites, National Satellite Meteorological Center (National Center for Space Weather), Beijing 100081, China

<sup>2</sup> College of Geoscience and Surveying Engineering, China University of Mining and Technology-Beijing, Beijing 100083, China

*Correspondence to:* Lin Zhu (zhulin@cma.gov.cn)

**Abstract.** The Hyperspectral Infrared Atmospheric Sounder Type II (HIRAS-II) aboard the Fengyun 3E (FY-3E) satellite provides valuable data on the vertical distribution of atmospheric states. However, effectively extracting quantitative atmospheric information from the observations is challenging due to the large number of hyperspectral sensor channels, inter-channel correlations, associated observational errors, and susceptibility of the results to influence by trace gases. This study explores the potential of FY-3E/HIRAS-II to atmospheric loadings of SO<sub>2</sub> from volcanic eruptions. A methodology for selecting SO<sub>2</sub> sensitive channels from the large number of hyperspectral channels recorded by FY-3E/HIRAS-II is presented. The methodology allows for the selection of SO<sub>2</sub>-sensitive channels that contain similar information on variations in atmospheric temperature and water vapor for minimizing the influence of atmospheric water vapor and temperature to SO<sub>2</sub>. A sensitivity study shows that the difference in brightness temperature between the experimentally selected SO<sub>2</sub> sensitive channels and the background channels efficiency removes interference signals from surface temperature, atmospheric temperature, and water vapor during SO<sub>2</sub> detection and inversion. A positive difference between near-surface atmospheric temperature and surface temperature enables the infrared band to capture more SO<sub>2</sub> information in the lower and middle layers. The efficiency of FY-3E/HIRAS-II SO<sub>2</sub> sensitive channels in quantitatively monitor volcanic SO<sub>2</sub> is demonstrated using data from the 29 April 2024 eruption of Mount Ruang in Indonesia. Using FY-3E/HIRAS-II measurements, the spatial distribution and qualitative information of volcanic SO<sub>2</sub> are easily observed. The channel selection can significantly enhance the computation efficiency while maintain the accuracy of SO<sub>2</sub> detection and retrieval, despite the large volume of data.

## 1 Introduction

Volcanoes pose significant threats to human populations around the world. During eruptions, they release a variety of gases (e.g., CO<sub>2</sub> and SO<sub>2</sub>), liquids (e.g., H<sub>2</sub>O and H<sub>2</sub>SO<sub>4</sub>), and solids (e.g., glass, minerals, and salts), with far-reaching environmental and climatic impacts (Patrick et al., 2020). Understanding the vertical distributions of these substances is essential to analyzing their atmospheric reactions (Bauduin et al., 2017).

Sulfur dioxide (SO<sub>2</sub>) is a magmatic volatile that is critical to volcanic geochemical analysis and hazard assessment due to its low ambient concentration, high abundance in volcanic plumes, and distinct spectral characteristics (Schmidt et al., 2012). The 1991 eruption of Mount Pinatubo and the 2014 eruption of Mount Bárðarbunga are both significant volcanic SO<sub>2</sub> eruption events, each producing SO<sub>2</sub> plumes exceeding  $1 \times 10^{10}$  kg (Shibata & Kinoshita, 2015). The 1991 Pinatubo eruption in particular produced a plume that peaked at 40 km height, resulting in the largest atmospheric aerosol event since the 1883 Krakatoa eruption (Holasek et al., 1996). Similarly, the 1982 eruption of El Chichón released approximately  $7.5 \times 10^9$  kg of SO<sub>2</sub> into the atmosphere, reaching 31 km in height (Carey & Sigurdsson, 1986). Tropospheric volcanic SO<sub>2</sub> and its transformation products affect the environment, human health, air quality, and the Earth's radiation balance (Gíslason et al., 2015). Hence, systematic monitoring of volcanic SO<sub>2</sub> emissions is essential.

Satellite radiometry offers significant advantages for this purpose, including long-term continuity and extensive spatial coverage (Krueger et al., 2009). Ultraviolet (UV) band sensors are limited to monitoring SO<sub>2</sub> from daytime eruptions due to their reflective nature. In contrast, general infrared (IR) sensors, with their broader channels, may filter out some SO<sub>2</sub> spectral information (Watson et al., 2004). Different techniques have been developed which make use of satellite-based broadband IR channels to detect volcanic SO<sub>2</sub> plume (Corradini et al., 2021; Corradini et al., 2010; Doutriaux-Boucher & Dubuisson, 2009; Prata & Kerkmann, 2007; Prata et al., 2004; Tournigand et al., 2020). It is found that the strong absorption at 7.3 μm is heavily affected by low level water vapor and thus this channel is usually used to retrieve SO<sub>2</sub> that is high (>3 km) in the atmosphere, and hence above most of the water vapor (Taylor et al., 2018). In addition, the retrieval is also very sensitive to uncertainties on surface temperature and emissivity (Corradini et al., 2009). Meanwhile, wide spectral channels are not sensitive enough to instantaneous changes in SO<sub>2</sub> composition, which will increase the minimum concentration of SO<sub>2</sub> components that can be monitored (Carn et al., 2003). Hyperspectral IR sensors enable observations with finer channel bandwidths that accurately characterize and distinguish each component, thereby reducing interference from other materials (Milstein & Blackwell, 2016). Although hyperspectral IR sensors provide thousands of spectral channels, they cannot all be used simultaneously for near real-time (NIR) operations owing to unmanageable data volumes and high computational burdens (Li & Han, 2017). At the same time, substantial redundancy and correlation mean that not all channels need to be considered. In addition, the low spectral resolution of traditional multispectral sensors makes it difficult for them to distinguish many important targets (Kruse, 2004) and is limited in quantitative calculations (Feng et al., 2006), thus reducing detection and retrieval accuracy.

To improve computational efficiency and detection accuracy, and to achieve rapid and accurate data acquisition require the selection of a set of channels that provide the maximum amount of information for specific applications (Chang et al., 2020). Rabier et al. (2002) proposed the “constant” iteration method for channel selection for the Infrared Atmospheric Sounding Interferometer (IASI) under clear-sky conditions, which maximized the information for applications. Fourrié and Rabier (2004) selected IASI channels for cloud-sensitive regions based on entropy reduction, demonstrating the robustness of the method. Gambacorta and Barnet (2013) used a physical approach to select channels based solely on their spectral characteristics, emphasizing spectral purity, avoiding redundancy, vertical sensitivity, low instrument noise, and global optimality. Lipton (2003) developed a method to select atmospheric microwave sounding channels based on the combination of each channel's

center frequency, bandwidth, and degrees of freedom for the signal, with both applicability to multiple environmental conditions and providing robust retrieval performance taken into consideration. Noh et al. (2017) employed the channel score index to individually evaluate channels selected using a one-dimensional variational (1Dvar) assimilation method. They used entropy subtraction for a comparative study of the selected channels, significantly reducing water vapor errors in the upper troposphere. Ventress and Dudhia (2014) proposed a 1Dvar method for selecting IASI channels and compared it with the method currently employed to choose channels for numerical weather prediction; their method reduced the sensitivity of the channel set to unknown spectral correlations while maintaining the same number of degrees of freedom for the signal. As information entropy iterative techniques do not consider the dynamic impacts of measurements throughout time and only account for the reduction in atmospheric state uncertainty from a single measurement, Di et al. (2022) developed an alternative approach to channel selection for the geostationary hyperspectral IR sounder by incorporating an M-index that considers temporal variations in the variance of the Jacobian. The adapted algorithm improved the accuracy of water vapor profile inversion.

The Jacobian function reflects the sensitivity of the radiation measured at a given pressure level in the atmosphere to changes in substance concentration (Di et al., 2016). In this paper, we propose a channel selection method based on the Jacobian matrix for SO<sub>2</sub> detection and retrieval using the Infrared Hyperspectral Atmospheric Vertical Sounder Type II (HIRAS-II) instrument onboard the Fengyun 3E (FY-3E) satellite.

The remainder of this paper is organized as follows. Section 2 details the data, the radiative transfer principle, and the radiative transfer model employed. Section 3 outlines the methodology of utilizing the Jacobian matrix to select sensitive and background channels for SO<sub>2</sub> monitoring. Section 4 investigates the effects of surface temperature and near-surface air atmospheric temperature variations on SO<sub>2</sub>, as well as the sensitivity of detecting SO<sub>2</sub> plumes in the preferred channels. Section 5 demonstrated a case study of Mount Ruang on the comparison of the effectiveness of SO<sub>2</sub> detection between the preferred channels and other absorption channels. Finally, section 6 provides a summary and discussion of the main findings.

## 2 Model and data

### 2.1 Radiative transfer model

The radiation observed by instruments at the top of the atmosphere (TOA) is modulated by the physical properties of both the atmosphere and Earth's surface (Aires et al., 2002). The atmospheric radiative transfer equation is a fundamental framework that governs the behavior of solar electromagnetic radiation and thermal radiation from both the atmosphere and the surface. It is crucial to analyzing radiative transfer processes and understanding atmospheric physical parameters (Seidel et al., 2010). In the absence of scattering and assuming local thermal equilibrium, the atmospheric radiative transfer equation in the IR band can be formulated as follows:

$$R = \varepsilon B_s(T_s)\tau_s - \int_0^{P_s} B(T)d\tau + (1 - \varepsilon) \int_0^{P_s} B(T)d\tau^* + 2.16 \times 10^{-5} \pi \cos \theta \times \rho_r B_r(T_{sun}) \times \tau_s^2, \quad (1)$$

where  $R$  represents spectral radiation,  $B$  is the Planck function at pressure level  $P$ ,  $\tau$  is total atmospheric transmittance above pressure level  $P$ ,  $\varepsilon$  is surface emissivity,  $T_s$  is surface temperature,  $T$  is the true atmospheric temperature,  $\theta$  is the zenith angle,  $\rho_r$  is solar reflectivity,  $T_{sun}$  is solar temperature, and define  $\tau^* = \tau_s^2 / \tau$ , (Li, 1994). Among them, subscript  $s$  represents surface skin and subscript  $r$  represents solar radiation. The term  $R$  represents the radiation reaching the satellite. The right-hand side of the equation has four components. The first is the surface emission term, which describes the radiation emitted from the surface that is transmitted through the atmosphere to the satellite. The second term accounts for the upward atmospheric radiation. The third captures the contribution of downward atmospheric radiation reflected from the surface to the satellite. The fourth term represents the contribution of solar radiation to the IR band, which can be neglected here because our focus is on the mid-wave and long-wave IR regions.

To calculate the TOA radiation using Eq. (1), the atmosphere is typically discretized into multiple layers, whose average properties (e.g., temperature, pressure, and molecular species) can be determined. Radiative transfer models facilitate this by allowing precise computation of radiation transmitted through atmospheric gases.

This study uses the Line-By-Line Radiative Transfer Model (LBLRTM), which is a sophisticated, vectorized model derived from Fast Atmospheric Signature Code. LBLRTM can accurately compute atmospheric fluxes and heating rates, making it well-suited to retrieving atmospheric temperature profiles and trace gas concentrations from high-resolution spectral radiance data (Clough, 1994). LBLRTM allows for the input of user-defined atmospheric profile files. In this study, the meteorological data input into LBLRTM consists of six standard atmospheric profiles: the 1976 US Standard Atmosphere, as well as profiles for mid-latitude summer, mid-latitude winter, subarctic summer and subarctic winter (Krueger & Minzner, 1976). These profiles provide 99 vertical levels of atmospheric parameters such as temperature, water vapor concentration, and  $SO_2$ .

Additional inputs include surface temperature, satellite zenith angle, and specific spectral band information, which are essential to calculating the simulated radiance and the Jacobian matrix. Given the spectral absorption characteristics of water vapor, temperature, and  $SO_2$  in the IR region, this study focuses on the mid- and long-wave IR bands observed by FY-3E/HIRAS-II.

## 2.2 FY-3E/HIRAS-II data

The FY-3E meteorological satellite is the world's first civilian dawn–dusk orbiting meteorological satellite (Zhang et al., 2022). It is part of China's second-generation polar-orbiting meteorological satellite series. Launched in July 2021, it delivers global cross-spectral atmospheric temperature and humidity vertical distribution data twice daily, in the morning and evening. Working at an inclination of  $98.75^\circ$  and altitude of 836 km, FY-3E completes 14 orbits around the Earth's poles each day, with each orbit taking  $\sim 101.5$  min, thus achieving comprehensive global coverage after 14 orbits. The satellite's HIRAS-II sensor features 3053 IR channels: 834 long-wave, 1207 mid-wave, and 1012 short-wave. Its measurements span a continuous spectrum range of  $648.75$  to  $2551.25 \text{ cm}^{-1}$  at a resolution of  $0.625 \text{ cm}^{-1}$ . Each infrared band contains  $3 \times 3$  detector arrays, which simultaneously observe the target area. A complete scanning cycle of HIRAS-II lasts 8 s, the instantaneous field of view (FOV) of each detector to the ground is  $1.1^\circ$ , Fig.1 is a schematic diagram of the field of view (Li et al., 2023). Based on the radiometric specifications for FY-3E/HIRAS-II, the noise equivalent target brightness temperature (BT) difference (NEdT) is

specified within 0.2 – 0.4 K for the long-wave IR band, 0.2 – 0.3 K (at 280 K) for the mid-wave IR band and 0.8 – 2.4 K (at 280 K) for the short-wave IR band (Huang et al., 2023). Overall, it delivers high-resolution IR spectra of the ground-atmosphere system. FY-3E/HIRAS-II data are freely available from the FENGYUN Satellite Data Service (<https://satellite.nsmc.org.cn/DataPortal/cn/home/index.html>).

Table 1 Spectral parameters of FY-3E/HIRAS-II channels (Xie et al., 2023)

IR Wave Band	Spectral Range (cm <sup>-1</sup> )	No. of Channels	Spectral Resolution (cm <sup>-1</sup> )
Long	648.75 – 1169.375 (15.41 – 8.55 μm)	834	0.625
Mid	1167.5 – 1921.25 (8.56 – 5.20 μm)	1207	0.625
Short	1919.375 – 2551.25 (5.21 – 3.92 μm)	1012	0.625

In practical applications, the Level 1 (L1) observation data from HIRAS-II require apodization to mitigate sidelobe effects (Xie et al., 2023). This is accomplished in the present study using the Hamming window function. In addition, radiometric measurements are typically integrated over a wavenumber interval and modified by the instrument’s line shape (Crevoisier et al., 2003). Consequently, we convolve the simulated brightness temperature (BT) with the FY-3E/HIRAS-II spectral response function to facilitate subsequent channel selection.

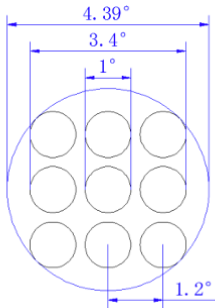


Figure 1: HIRAS-II detector distribution and corresponding ground field of view.

### 2.3 Sentinel-5P/TROPOMI SO<sub>2</sub> data

Sentinel-5P is a quasi-polar, sun-synchronous satellite in a low Earth orbit with a height of about 824 km, and it covers the entire planet each day (van Geffen et al., 2020). Every orbital period lasts 16 days, with an average of 227 orbits every period (14 orbits per day) (Corradino et al., 2024). The satellite hosts the Tropospheric Monitoring Instrument (TROPOMI). Daily or sub-daily revisits of specific sites are achievable, given TROPOMI’s 108° cross-orbit field of view and its ability to capture data across multiple orbits (Theys et al., 2017). Since 2019, Sentinel-5P’s spatial resolution has been enhanced to

145 3.5 km × 5.5 km. TROPOMI measures data across four spectral regions (ultraviolet, visible, near-infrared, and shortwave infrared) and is adept at monitoring SO<sub>2</sub> and a range of other gases (Theys et al., 2019). With a comparable footprint of 12 km diameter, TROPOMI demonstrates greater sensitivity to SO<sub>2</sub> variations than IASI (Cofano et al., 2021).

This study uses TROPOMI's Level 2 (L2) geophysical SO<sub>2</sub> products, accessible through the European Space Agency's Copernicus Open Access Center via the Sentinel-5P Pre-Operations Hub. We are using the offline (OFFL) data of this version, 150 which are freely available (Copernicus Sentinel-5P, 2020). These L2 products are derived from Level 0 (L0) raw data, which undergo calibration and georeferencing, followed by processing to Level 1b (L1b) data, including brightness and irradiance. In this study, Sentinel-5P/TROPOMI SO<sub>2</sub> data are primarily employed to validate the SO<sub>2</sub> detection capabilities of FY-3E/HIRAS-II at Mount Ruang (Inness et al., 2022).

## 2.4 Atmospheric profile data

155 This study employs standard atmospheric profile data as inputs for the LBLRTM. The profiles used are the US Standard Atmosphere, 1976, and tropical, mid-latitude summer and winter, subarctic summer and winter profiles. The US Standard Atmosphere, 1976, serves as an idealized stable representation of Earth's atmosphere from the surface to 1000 km, detailing the relative changes in atmospheric composition with altitude. Below 86 km, the atmospheric composition is calculated using a series of linear functions, while the upper region is defined by continuous functions that closely approximate observational 160 data (Krueger & Minzner, 1976).

ERA5 is the latest comprehensive reanalysis dataset from the European Centre for Medium-Range Weather Forecasts (ECMWF), superseding ERA-Interim. With daily updates, ERA5 provides hourly estimates of the world's atmosphere, land surface, and waves in the ocean from 1950 onward (Hersbach et al., 2020). Each profile from ERA5 has a horizontal scale of 31 km. This includes upper-air parameters on 37 fixed pressure levels from 1,000 to 1 hPa and 137 model levels distributed 165 using hybrid sigma-pressure coordinate system. For this study, we interpolate ERA5 400 hPa fixed pressure level data to assess atmospheric water vapor conditions near Mount Ruang concurrent with FY-3E/HIRAS-II observations.

## 3 Channel selection method

When selecting channels, it is crucial to avoid bands with cloud or aerosol interference and long-wave channels that provide redundant information (Tsuchiya, 1983). In addition, as the temperature Jacobian matrices of the water vapor and ozone 170 channels can be strongly influenced by the state of the atmosphere, they should not be used as the main sources of temperature information (Kuai et al., 2010). Therefore, different sets of channels should be considered at various stages during the channel selection process. This research suggests two primary steps for channel selection, as follows.

1. Initially, channels are excluded through pre-screening, which eliminates regions of high uncertainty in the simulated spectrum based on specific criteria.

175 2. The primary channel selection algorithm is based on Jacobian calculations as a measure of the information content of various atmospheric species and is executed through multiple independent selection operations.

3.1 Channel pre-screening

Channel pre-screening rejects spectral regions that would bring substantial uncertainty in the subsequent simulation phase, thus enhancing the efficiency of and reducing data redundancy in the forward simulations (Li et al., 2022). We pre-screened the mid- and long-wave IR bands by eliminating trace gas absorption channels and applying a threshold to the noise equivalent target brightness temperature (BT) difference (NEdT).

The first step eliminates channels with strong absorption of trace gases. For any of the six standard atmospheric profiles, channels are removed if changes in trace gas content induce a BT shift of >1 K. Channels are retained if the gas-induced BT change is <1 K; the influence of these gases is then incorporated into the forward model for simulation. Among nine trace gases (CH<sub>4</sub>, CO, N<sub>2</sub>O, CCl<sub>4</sub>, CFC-11, CFC-12, CFC-14, HNO<sub>3</sub>, NO<sub>2</sub>, OCS, and NO), only the first three significantly affect the channel BT (Collard, 2007). As the absorption bands of CO and N<sub>2</sub>O fall outside this study’s spectral range, we focus on CH<sub>4</sub> for testing. Channels significantly influenced by ozone and solar irradiance are also excluded.

The second step involves eliminating channels with excessive noise. To minimize the risk of excluding relevant spectral bands or retaining inappropriate bands, a threshold of 0.2 K for NEdT is adopted as the pre-screening criterion for channel selection.

190 The third step excludes channels with non-linear Jacobian matrix and multiple Jacobian peaks. Using the LBLRTM model and six standard atmospheric profiles, we calculate the Jacobian matrix for temperature and water vapor. Channels exhibiting significant double or multiple peaks in the Jacobian matrix are excluded. Figure 2 illustrates the channels rejected during pre-screening: the red areas indicate channels influenced by O<sub>3</sub>, purple areas are those affected by CH<sub>4</sub>, and yellow areas those with multiple peaks in the Jacobian matrix.

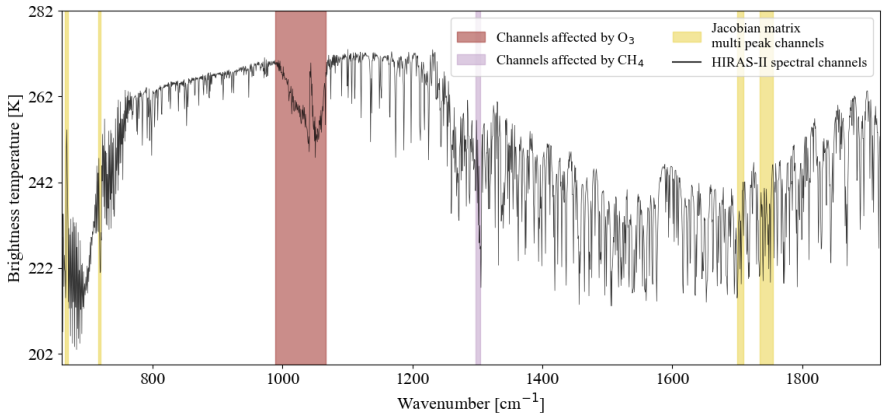


**Figure 2: FY-3E/HIRAS-II channel pre-screening results: red and purple highlight channels affected by O<sub>3</sub> and CH<sub>4</sub>, respectively; yellow highlights channels with multiple peaks in the Jacobian matrix.**

### 195 3.2 Jacobian matrix based information analysis

We calculate and analyze the information generated by water vapor, temperature, and SO<sub>2</sub> at different altitudes to select and utilize the most relevant channels. To evaluate the capability of HIRAS-II channels to provide information on these parameters, we employ the Jacobian matrix for channel selection. The Jacobian functions can identify a set of optimal channels with maximum or minimum information content for each atmospheric profile. It assesses the sensitivity of radiation to the specific  
200 physical and chemical parameters. For a specified wavenumber ( $\nu$ ), the sensitivity of BT to variations in geophysical parameters ( $X$ ) is represented by the Jacobian matrix for each pressure layer (Coopmann et al., 2020) as follows:

$$J_{\nu}(X) = \frac{\partial BT(\nu)}{\partial X}, \quad (2)$$

The Jacobian matrix illustrates the sensitivity of atmospheric BT to temperature, humidity, and various gas concentrations at a given wavenumber (Aires et al., 2016).

205 Three key parameters for measuring the properties of a Jacobian matrix are employed. The first parameter is the maximum value of each Jacobian matrix, denoted as  $M$ , quantifies the information (here, all discussions of  $M$  in this paper only consider its maximum value, i.e.,  $|M|$ ). The second is the pressure level  $P$  corresponds to the height where the Jacobian matrix attains its peak value, indicating the altitude at which the IR radiation is the most responsive to variations in atmospheric composition. The third parameter,  $dP$ , represents the width at half maximum of the Jacobian matrix peak, defined as the pressure difference  
210 between the two levels where the Jacobian matrix value drops to half of its maximum. This metric represents the vertical extent of the atmospheric layer contributing most significantly to the IR signal. Figure 3 schematically represents the SO<sub>2</sub> profile, the Jacobian peak and the maximum half-width of the Jacobian function under the conditions of the US standard atmosphere, 1976.



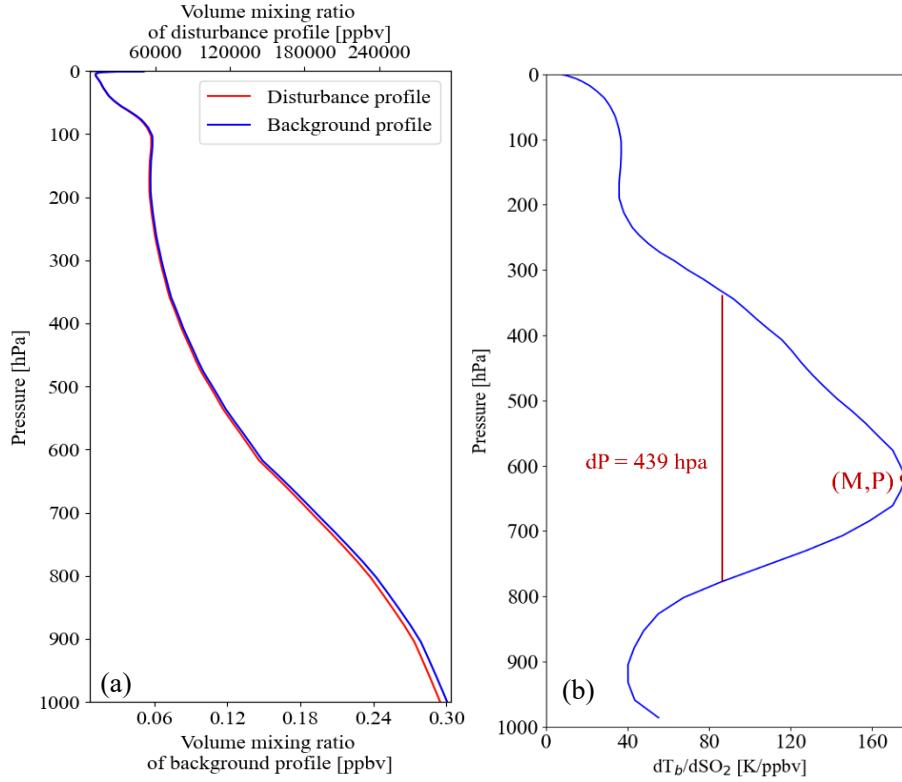


**Figure 3: Representation of the maximum half-width and peak value of the SO<sub>2</sub> Jacobian function for the US Standard Atmosphere, 1976: (a) SO<sub>2</sub> profile, (b) 1163.125 cm<sup>-1</sup> channel.**

To accurately monitor SO<sub>2</sub>, it is essential to minimize the interference of atmospheric temperature and water vapor on the SO<sub>2</sub> channels. Since the radiance signals from SO<sub>2</sub> channels are simultaneously influenced by atmospheric temperature, water vapor, and SO<sub>2</sub>, it is necessary to utilize other channels to provide independent atmospheric temperature and water vapor information for separation. In selecting channels minimally influenced by atmospheric temperature, we prioritize those channels that are primarily sensitive to a single gas with a constant concentration, CO<sub>2</sub> absorption channels primarily reflect the information of atmospheric temperature profiles (Li et al., 2022). Consequently, we utilize the spectral absorption region of CO<sub>2</sub> (666 – 1000 cm<sup>-1</sup>) to calculate the temperature Jacobian matrix and combine this with the atmospheric IR window channel to select the atmospheric temperature channels. Water vapor channels contain both temperature and water vapor information, while SO<sub>2</sub> channels contain information of temperature, water vapor and SO<sub>2</sub>. To separate temperature from water vapor in water vapor absorption channel radiances, CO<sub>2</sub> channels play an important role through providing temperature information. If a water vapor absorption channel and a CO<sub>2</sub> absorption channel have similar temperature Jacobian, they have also similar temperature sensitivity, and thus that CO<sub>2</sub> channel is helpful for separating the temperature from water vapor in the water vapor channel radiance. Same for a SO<sub>2</sub> channel, if a water vapor channel has similar temperature Jacobian and water vapor Jacobian, then the water vapor channel is helpful for separating temperature and water vapor from SO<sub>2</sub> in that SO<sub>2</sub> channel radiance. During the cross-comparison of channel selection, we ensure that the water vapor Jacobian matrix and temperature Jacobian matrix

within the water vapor absorption region are consistent with those in the SO<sub>2</sub> channels. Thus, when subtracting the brightness temperature of the SO<sub>2</sub> channels from that of the water vapor channels, the influence of water vapor, atmospheric temperature, and surface radiation shared by both channels can be effectively removed.

The specific channel selection process is shown in Fig. 4, it illustrates the cross-comparison process using the three key parameters of Jacobian matrices in the range of SO<sub>2</sub>, water vapor and CO<sub>2</sub> absorption regions. Initially, we computed the temperature, water vapor, and SO<sub>2</sub> Jacobian matrix for the six standard atmospheric profiles. Then, the similarity in the peak and half-width of the Jacobian matrix at specific pressure level P for HIRAS-II channels in SO<sub>2</sub>, water vapor and temperature absorption region were cross-compared. The temperature Jacobian information for the atmospheric temperature channels and the water vapor Jacobian information for the water vapor channels needs to align with that for the SO<sub>2</sub> channels to minimize the influence of atmospheric water vapor and temperature to SO<sub>2</sub>. Similarly, the temperature and water vapor Jacobian information for the water vapor channels must match the corresponding information for the SO<sub>2</sub> channels. Consequently, when SO<sub>2</sub> concentration changes, the similarity of the water vapor and temperature Jacobian matrices between the SO<sub>2</sub> channels and the water vapor channels can effectively eliminate the interference of atmospheric temperature and water vapor on SO<sub>2</sub> monitoring results.

Using this information, we then identified the atmospheric temperature channels, water vapor absorption channels, and SO<sub>2</sub>-sensitive channels. Considering the variability in the sensitivity of the HIRAS-II channels to the atmospheric conditions, we utilize 1040 hPa as the near-surface atmospheric pressure and compute the Jacobian matrices for water vapor, temperature, and SO<sub>2</sub> across 99 vertical atmospheric sections of the six atmospheric profiles.

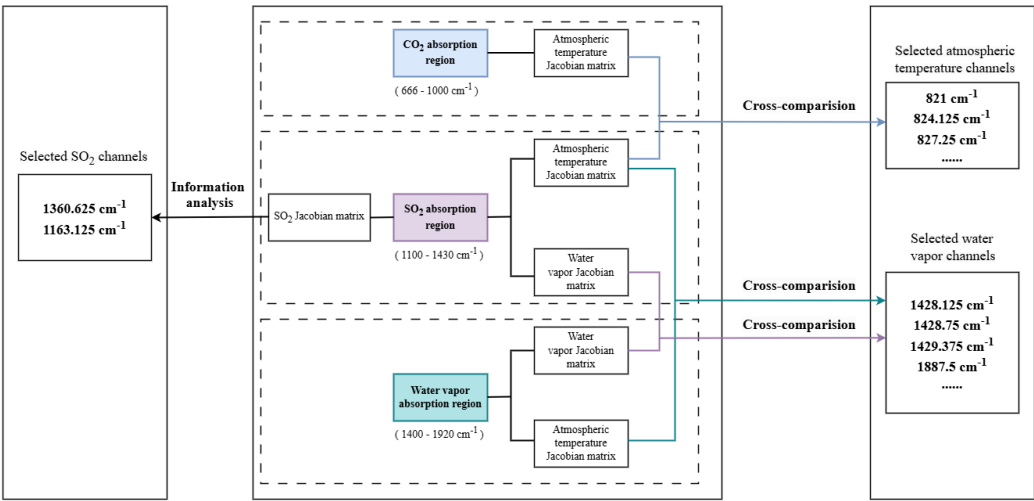
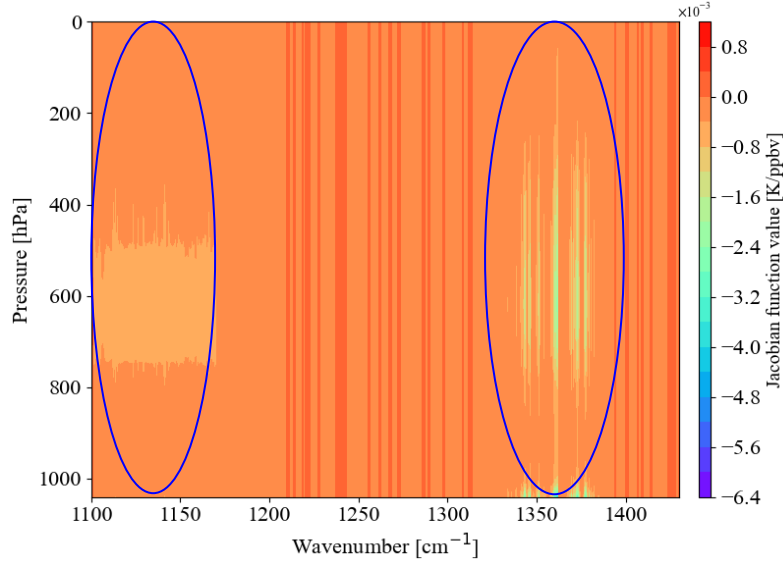


Figure 4: Schematic diagram of channel selection method.

### 3.2.1 SO<sub>2</sub> channel selection

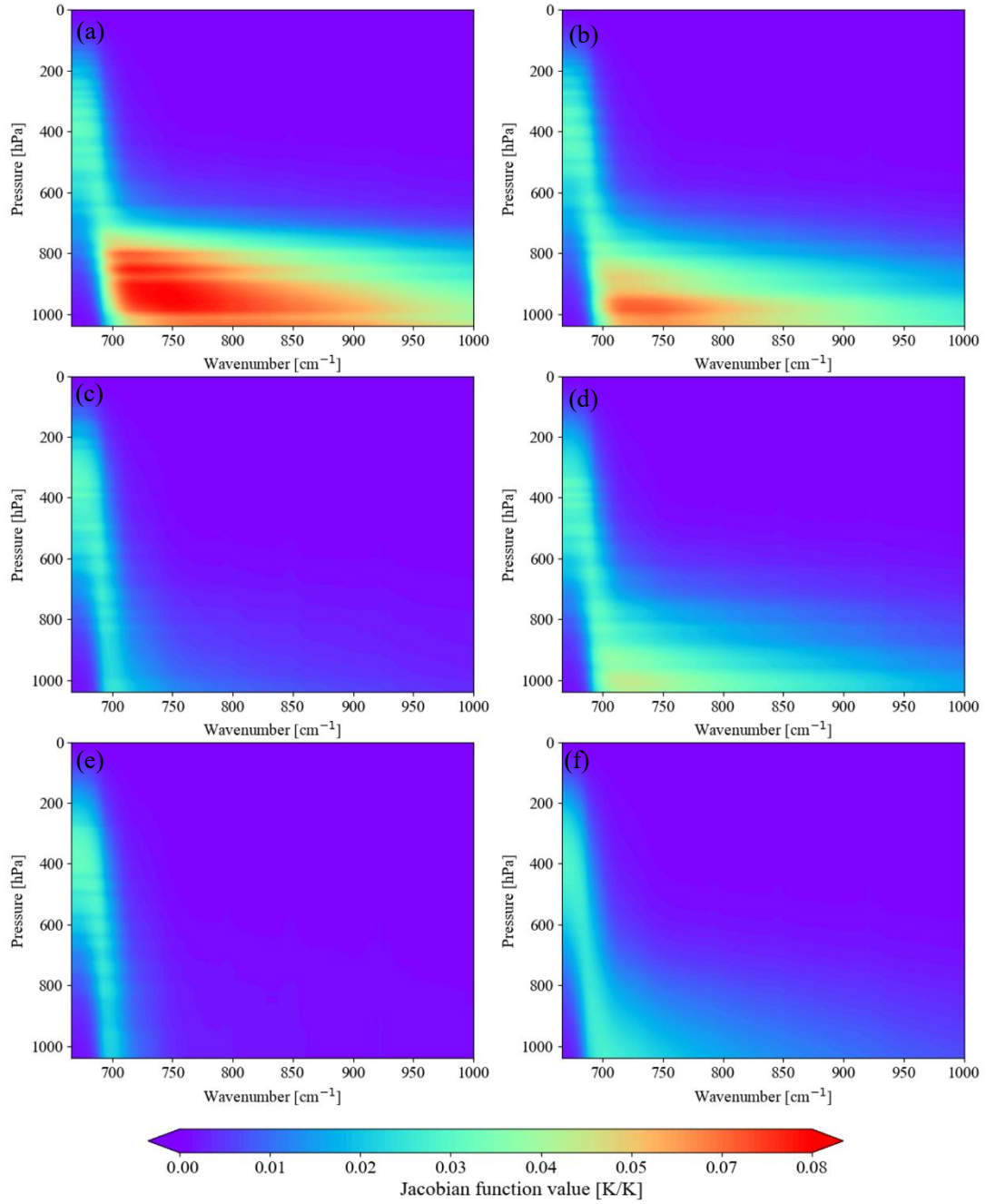
In situ measurements reported by Rose et al. (2004) indicate SO<sub>2</sub> concentrations of 500 – 1000 ppbv during an aircraft encounter with a 35-hour-old volcanic plume from the Icelandic Hekla eruption in February 2000, at a distance of approximately 1300 km from the source. In comparison, the concentration of SO<sub>2</sub> in the clean troposphere typically ranges from 0.25 – 0.43 ppbv (Casadevall et al., 1984). Given that SO<sub>2</sub> concentrations increase dramatically over a short period during volcanic eruptions, for SO<sub>2</sub>, we perturb the atmospheric profiles at different pressure levels using  $5 \times 10^4$  times gas content, to better represent the gas distribution characteristics in volcanic eruption scenarios. Given the low SO<sub>2</sub> content under the other five atmospheric conditions, this study focuses on the SO<sub>2</sub> information for the US Standard Atmosphere, 1976. The corresponding SO<sub>2</sub> Jacobian functions (Fig. 5) clearly shows that the SO<sub>2</sub> absorption region is located mainly around the central wavenumbers of 1360 and 1163 cm<sup>-1</sup>. The 1360 cm<sup>-1</sup> band exhibits the strongest SO<sub>2</sub> signal among the available spectral bands. However, it is also a strong absorption region for atmospheric water vapor, which can introduce contamination in SO<sub>2</sub> retrievals. This band demonstrates minimal sensitivity to radiative contributions from the surface and lower atmosphere, making it particularly effective for monitoring stratospheric SO<sub>2</sub> plumes (Thomas & Watson, 2010). In contrast, the 1163 cm<sup>-1</sup> band falls within an atmospheric window region. While the presence of SO<sub>2</sub> in this band leads to a certain degree of radiative attenuation, it remains well-suited for detecting SO<sub>2</sub> plumes in the troposphere (Carboni et al., 2016). This characteristic makes it especially valuable for monitoring volcanic activity characterized by continuous passive degassing. By leveraging the complementary strengths of these bands, we select SO<sub>2</sub>-sensitive channels with a central wavenumber around 1163 and 1360 cm<sup>-1</sup>. In addition, SO<sub>2</sub> absorption information is discernible at various altitudes in the atmosphere, particularly in the middle atmosphere and near the surface. To obtain pure SO<sub>2</sub> absorption information, it is essential to eliminate information about the surface temperature, atmospheric temperature, and water vapor that might interfere with the SO<sub>2</sub> observation channels, thereby avoiding overestimation or misestimation of the SO<sub>2</sub> content and dispersion trends. We selected the top channels with the highest Jacobian matrix values in the SO<sub>2</sub> absorption region near 1360 and 1163 cm<sup>-1</sup>, which are 1360.625, and 1163.125 cm<sup>-1</sup>. These two channels contain prominent SO<sub>2</sub> absorption information.



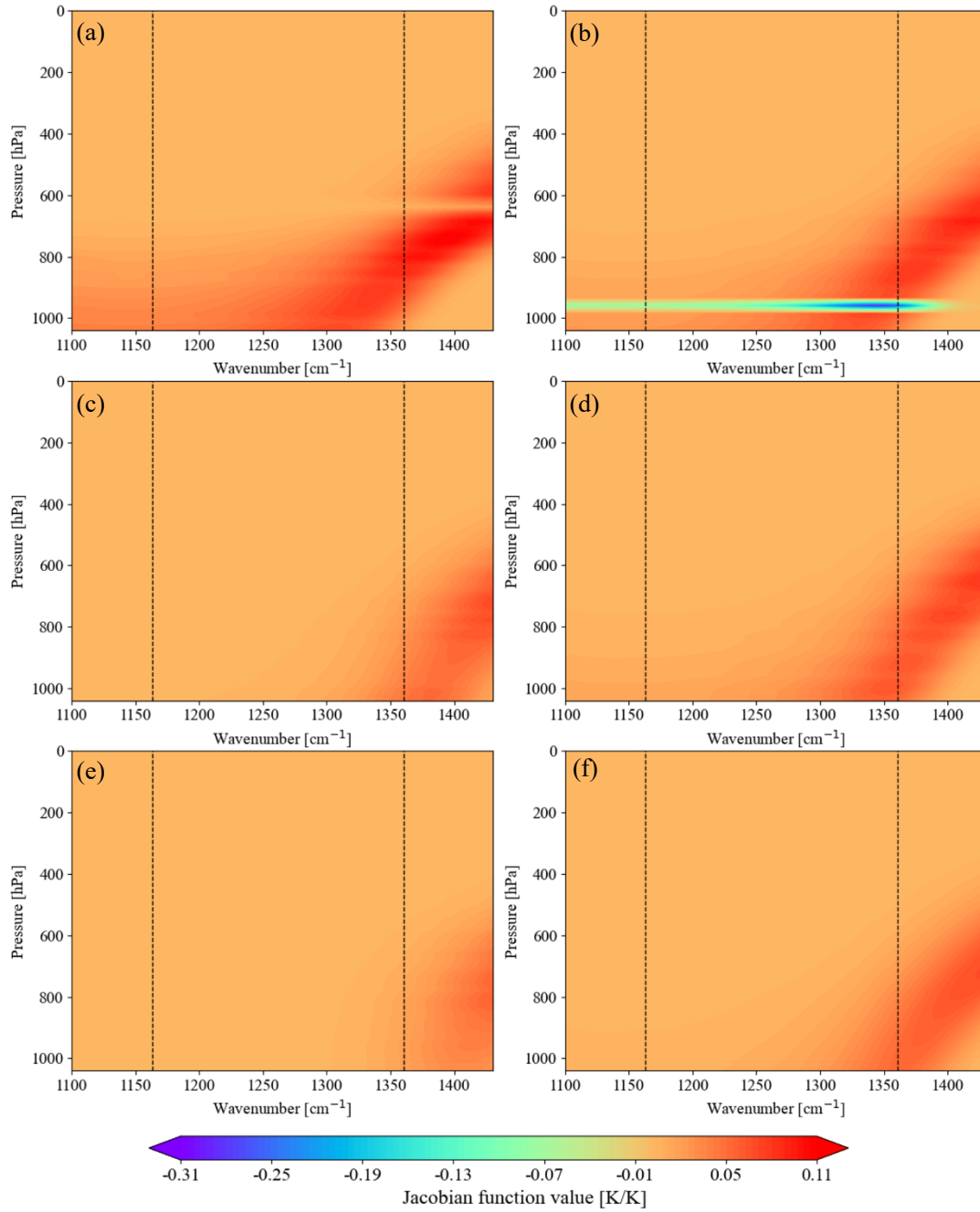
**Figure 5: Schematic diagram of the SO<sub>2</sub> Jacobian matrix with atmospheric profiles from the US Standard Atmosphere, 1976.**

### 3.2.2 Atmospheric temperature channel selection

Volcanic eruptions typically change the temperature of the stratosphere and troposphere, making it essential to eliminate any interference effect of atmospheric temperature on SO<sub>2</sub> observations (Yang & Schlesinger, 2002). Figure 6(a)-(f) shows temperature Jacobian functions for the six atmospheric profiles, revealing that near-surface temperatures are more responsive to temperature perturbations in the tropical, mid-latitude summer, subarctic summer, and US Standard Atmosphere, 1976, profiles, while the mid-latitude winter and subarctic winter profiles exhibit greater fluctuations at higher altitudes. For the atmospheric temperature channels, it is crucial that the temperature Jacobian functions peak at the same altitude as those of the SO<sub>2</sub> channels and have similar half-widths of their Jacobian functions. We compare the temperature Jacobian functions of the SO<sub>2</sub> channels with that of the atmospheric temperature absorption region under each set of atmospheric profiles, so that each channel in the atmospheric temperature absorption region can be compared with all channels in the SO<sub>2</sub> absorption region for atmospheric temperature absorption information. First, we filter out channels where both peak at the same altitude. Then we determine the final atmospheric temperature channels using a threshold of the half-width difference being <0.1. Channels meeting these conditions, along with the SO<sub>2</sub> channels, exhibit consistent temperature absorption information and adequately cover the atmospheric temperature channels for the six observed atmospheric conditions. According to Fig. 7, many channels in atmospheric temperature absorption region also have similar atmospheric temperature absorption information with multiple SO<sub>2</sub> channels at the same time.



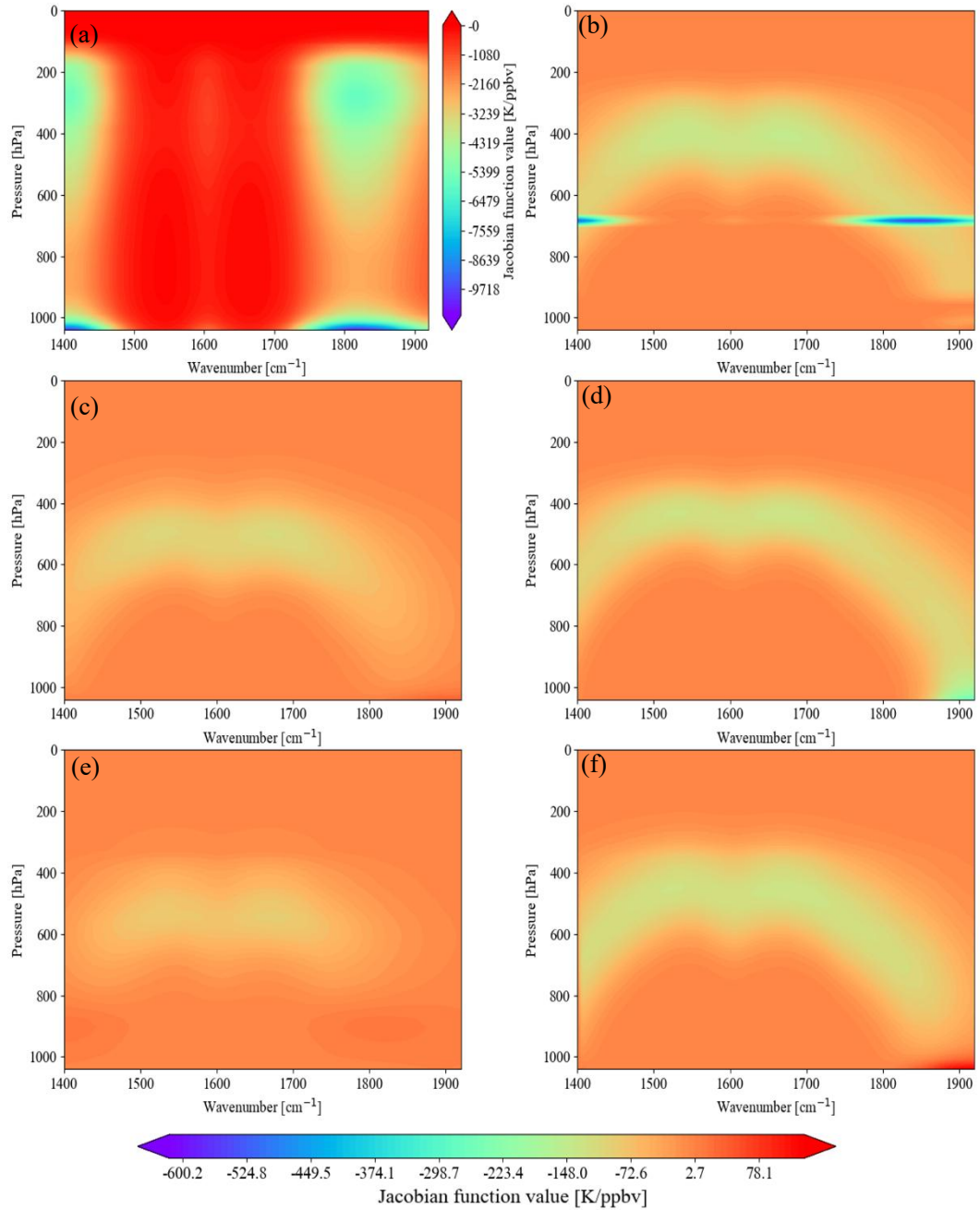
**Figure 6: Representations of temperature Jacobian functions at atmospheric temperature absorption region for the conditions of six atmospheric profiles: (a) tropical atmospheric profile, (b) mid-latitude summer atmospheric profile, (c) mid-latitude winter atmospheric profile, (d) subarctic summer atmospheric profile, (e) subarctic winter atmospheric profile, and (f) US Standard Atmosphere, 1976.**



**Figure 7: Representations of temperature Jacobian functions at SO<sub>2</sub> absorption region (black dashed lines represent selected SO<sub>2</sub> channels) for the conditions of six atmospheric profiles: (a) tropical atmospheric profile, (b) mid-latitude summer atmospheric profile, (c) mid-latitude winter atmospheric**

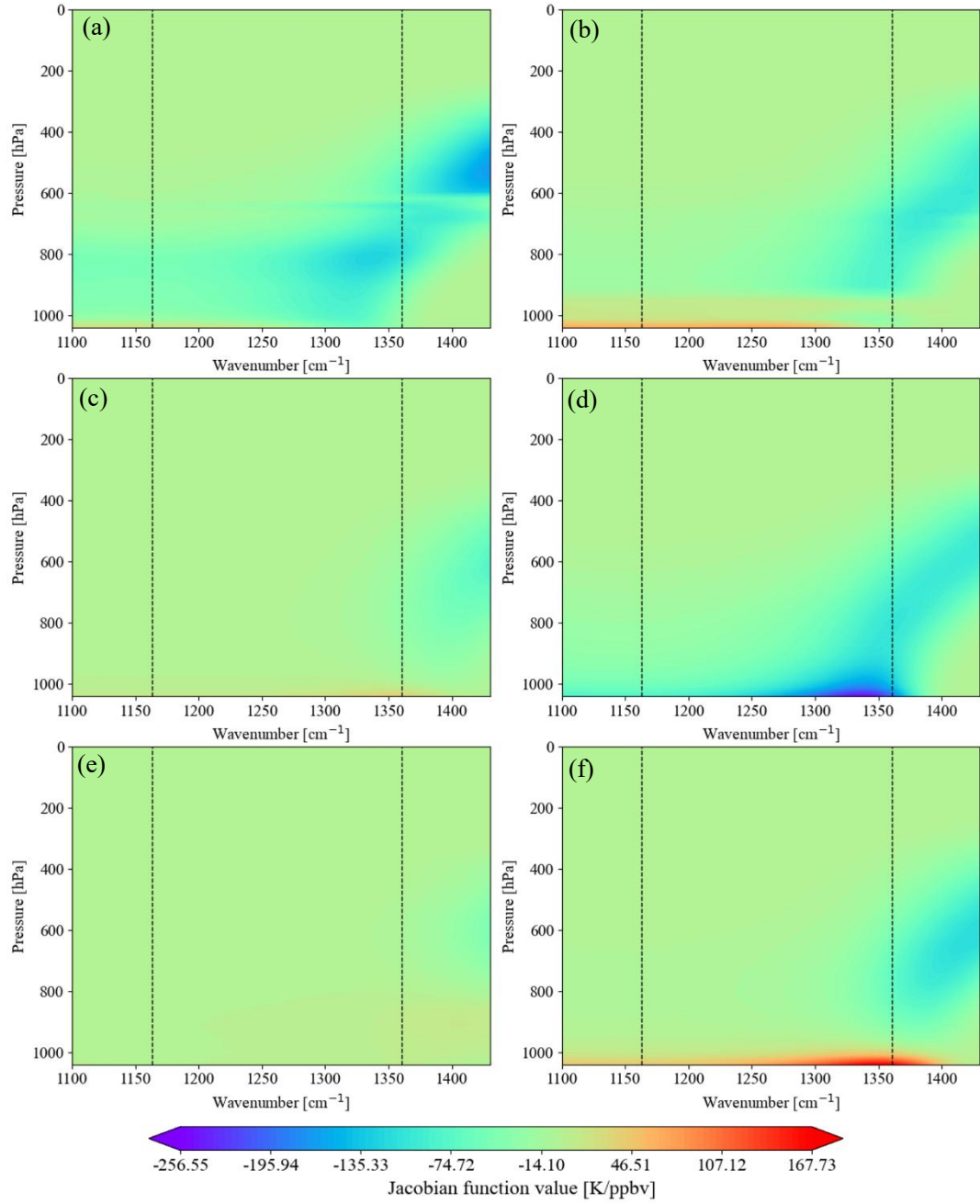
285 **3.2.3 Water vapor absorption channel selection**

Figure 8 shows strong absorption by water vapor around  $1428$  and  $1850\text{ cm}^{-1}$  under the six atmospheric conditions, indicating this region contains substantial absorption information on water vapor. In addition, the absolute value of the Jacobian function for water vapor in the lower and middle layers of the  $1428\text{ cm}^{-1}$  band can reach up to  $-9.7 \times 10^3\text{ K/ppbv}$  under the tropical, meanwhile, mid-latitude summer, subarctic summer, and 1976 US Standard Atmosphere profiles, indicating that water vapor  
290 has a stronger influence than in the mid-latitude winter and subarctic winter profiles. At the same time, it can be seen from Fig. 9 that the  $\text{SO}_2$  absorption region around  $1360\text{ cm}^{-1}$  is more susceptible to water vapor contamination than the  $1163\text{ cm}^{-1}$  absorption region. Under most atmospheric profile conditions, there exists a channel within the water vapor absorption region that exhibits Jacobian characteristics consistent with the selected  $\text{SO}_2$  channels according to Fig. 9. We calculate the temperature Jacobian functions and water vapor Jacobian functions separately within the water vapor absorption region and  
295  $\text{SO}_2$  absorption region. The Jacobian information of water vapor in  $\text{SO}_2$  and water vapor absorption region are cross compared. The Jacobian information of atmospheric temperature in  $\text{SO}_2$ , water vapor absorption region and selected atmospheric temperature channels are also cross compared and the channels with consistent maximum peak value and half-width were selected to ensure that the vertical changes of water vapor and atmospheric temperature were consistent with those of  $\text{SO}_2$ . The cross-comparison criteria of the Jacobian matrix here are consistent with the selection criteria and threshold of the  
300 atmospheric temperature channels in section 3.2.2. Through the cross-comparison process, the selected water vapor channels can simultaneously contain consistent atmospheric temperature and water vapor absorption information to the  $\text{SO}_2$  channels. In this way, the atmospheric temperature and water vapor absorption information carried in the selected  $\text{SO}_2$  channels can be removed in the subsequent calculation of the BT difference between the  $\text{SO}_2$  channels and the water vapor channels. Figure 10 illustrates the specific central wavenumbers of the selected atmospheric temperature channels, water vapor absorption  
305 channels and their corresponding BTs under the 1976 US Standard Atmosphere.



**Figure 8: Representations of water vapor Jacobian functions at water absorption region for conditions of six atmospheric profiles: (a) tropical atmospheric profile, (b) mid-latitude summer atmospheric profile, (c) mid-latitude winter atmospheric profile, (d) subarctic summer atmospheric profile, (e) subarctic winter atmospheric profile, and (f) US Standard Atmosphere, 1976.**





**Figure 9: Representations of water vapor Jacobian functions at SO<sub>2</sub> absorption region (black dashed lines represent selected SO<sub>2</sub> channels) for conditions of six atmospheric profiles: (a) tropical atmospheric profile, (b) mid-latitude summer atmospheric profile, (c) mid-latitude winter atmospheric profile, (d) subarctic summer atmospheric profile, (e) subarctic winter atmospheric profile, and (f) US Standard Atmosphere, 1976.**

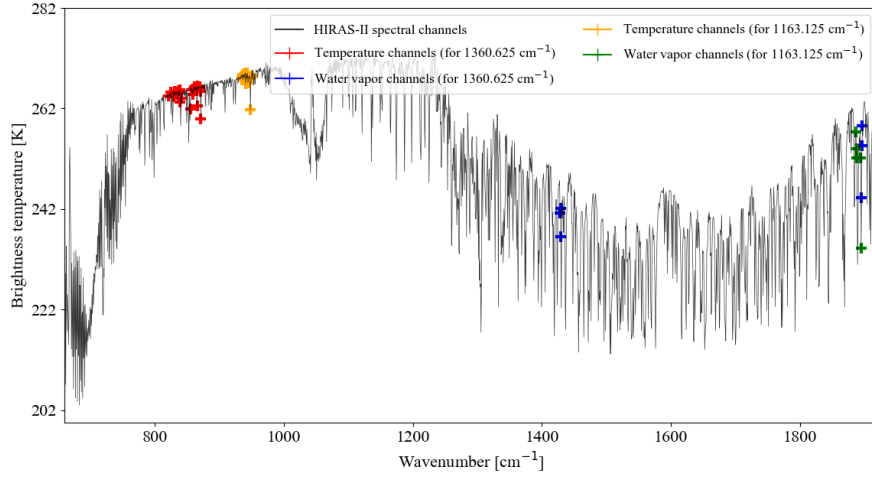


**Figure 10: Part of the HIRAS-II brightness temperature spectrum with selected atmospheric temperature channels and water vapor absorption channels labelled.**

Under the same  $\text{SO}_2$  and water vapor conditions and based on the selected  $\text{SO}_2$  channels, we respectively selected three corresponding water vapor channels for both the  $1163.125$  and  $1360.625 \text{ cm}^{-1}$  channels whose channel combination with the largest brightness temperature difference. By analyzing the BT difference, we determined the  $\text{SO}_2$  sensitive channels to accurately carry out the  $\text{SO}_2$  retrieval. As can be seen in Fig. 11,  $1163.125$  and  $1360.625 \text{ cm}^{-1}$  is used as the  $\text{SO}_2$ -sensitive channels,  $1887.5$  and  $1429.375 \text{ cm}^{-1}$  as the water vapor absorption channels. For  $1360.625 \text{ cm}^{-1}$  channel, the combination of the channels we chose can effectively remove the water vapor information contained in the  $\text{SO}_2$ -sensitive channels and can also better demonstrate the  $\text{SO}_2$  plume after deducting the effect of water vapor, which lays the foundation for the  $\text{SO}_2$  retrieval in the subsequent inversion process.

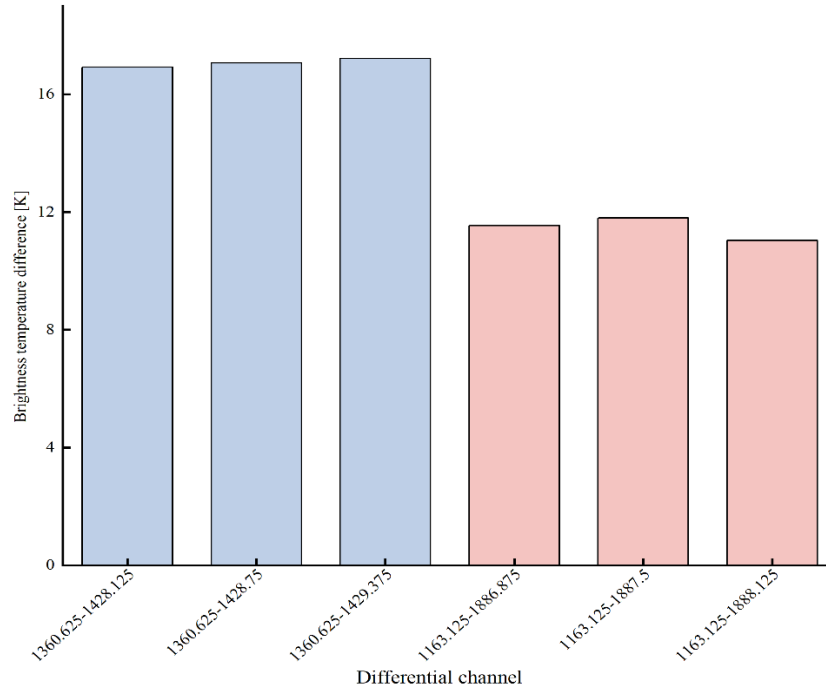


**Figure 11: Brightness temperature difference between SO<sub>2</sub> channel and water vapor absorption channel with atmospheric profiles from the 1976 US Standard Atmosphere.**

### 3.3 Surface temperature channel selection

Land surface temperature (or surface skin temperature) is a key variable in IR data inversion (Jimenez-Munoz et al., 2009). The atmosphere minimally reflects, scatters, and absorbs electromagnetic waves in the atmospheric IR window band (Senf & Deneke, 2017). Therefore, we select the clean channel from this range with the highest BT: its use in subsequent analyses as the land surface temperature channels mitigates the influence of land on SO<sub>2</sub> observations. Table 2 presents the distribution of the three channels with the highest BT across the six atmospheric profiles. Notably, the land surface temperature channels for the mid-latitude winter and subarctic winter situations are identical, while those for the mid-latitude summer and subarctic summer profiles are somewhat similar. The tropical atmosphere profile has a land surface temperature channel with a higher wavenumber and shorter wavelength compared with the other profiles. The land surface temperature channel for the US Standard Atmosphere, 1976, falls between those of the other profiles. To ensure the selected land surface temperature channels are applicable to most atmospheric conditions, we identify the two channels with the highest frequency (902.5 and 901.875 cm<sup>-1</sup>) for subsequent work.

Table 2 Distribution of surface temperature channels under six atmospheric profiles

Atmosphere profile	Channel wavenumber ( $\text{cm}^{-1}$ )		
Tropical	916.875	905.625	906.875
Midlat Summer	904.375	903.75	902.5
Midlat Winter	901.25	901.875	902.5
Subarctic Summer	904.375	901.875	902.5
Subarctic Winter	901.25	901.875	902.5
US1976	901.25	901.875	902.5

## 330 4 Sensitivity analysis

### 4.1 Effects of differences in surface temperature and near-surface atmospheric temperature on $\text{SO}_2$ -sensitive channels

Given the variations in surface characteristics affecting atmospheric radiation, we analyzed the impact of the generally low temperature difference between the surface and the overlying air on the  $\text{SO}_2$  Jacobian function. Meanwhile, the  $750 - 1200 \text{ cm}^{-1}$  region is highly sensitive to surface features (Clarisse et al., 2010), and the sensitivity of HIRAS-II to  $\text{SO}_2$  is significantly  
335 influenced by the temperature difference (TD) between the surface and the first distinct layer of air ( $T_p$ ) (Tsuchiya, 1983). The Jacobian formula defines the relationship between the change in brightness temperature and the perturbation in material concentration. Under consistent atmospheric conditions with fixed  $\text{SO}_2$  concentration perturbations and uniform background brightness temperature, the TD after  $\text{SO}_2$  perturbation demonstrates a similar trend and behavior to that of the Jacobian value. As a result, TD can effectively substitute for the Jacobian value in assessing the detection capability of  $\text{SO}_2$ . For simplicity,  
340 we consider three scenarios:  $T_s = T_p$  (TD = 0),  $T_p > T_s$  (TD > 0), and  $T_p < T_s$  (TD < 0). With  $\varepsilon = 0.98$  and  $P = 212 \text{ hPa}$ , TD was varied from  $-10$  to  $10 \text{ K}$  in  $5 \text{ K}$  increments, and infrared radiation was simulated under each set of conditions. Figure 12 illustrates variations in the  $\text{SO}_2$  plume in  $1163.125$  and  $1360.625 \text{ cm}^{-1}$  channels under different TD conditions for the US Standard Atmosphere, 1976.

From Fig. 12(a), it can be observed that for the  $1360.625 \text{ cm}^{-1}$  channel,  $\text{SO}_2$  with column densities  $<150 \text{ DU}$  exhibits high  
345 sensitivity to changes in the TD. However, when the  $\text{SO}_2$  column density  $>150 \text{ DU}$ , the response of TD to concentration variations significantly weakens, indicating that this channel tends to saturate at higher  $\text{SO}_2$  concentrations. This phenomenon demonstrates that the  $1360.625 \text{ cm}^{-1}$  channel is more effective for detecting  $\text{SO}_2$  in the middle and upper troposphere. In contrast, as shown in Fig. 12(b), for the  $1163.125 \text{ cm}^{-1}$  channel, a positive change in TD leads to a significant increase in brightness temperature at the same  $\text{SO}_2$  concentration. As the  $\text{SO}_2$  concentration increases, the influence of TD on brightness  
350 temperature decreases approximately linearly. This suggests that the  $1163.125 \text{ cm}^{-1}$  channel is more susceptible to interference from surface and near-surface radiation properties, with its signal primarily reflecting the distribution of  $\text{SO}_2$  in the lower atmosphere.

For a plume  $\text{SO}_2$  content of  $<150$  DU, an increasingly positive TD enhances  $\text{SO}_2$  detection in the IR band. Conversely, a decrease in TD limits  $\text{SO}_2$ 's contribution to radiation, thereby constraining its IR remote sensing capability. As the plume's  $\text{SO}_2$  content increases, the impact of TD on  $\text{SO}_2$  observation diminishes. These findings suggest that favorable TD conditions can enhance the accuracy of  $\text{SO}_2$  detection and inversion, which is relevant to monitoring air quality. Due to the vertical distribution of gases, near-surface  $\text{SO}_2$  tends to be underestimated, but a positive TD helps capture the net absorption of near-surface  $\text{SO}_2$ .

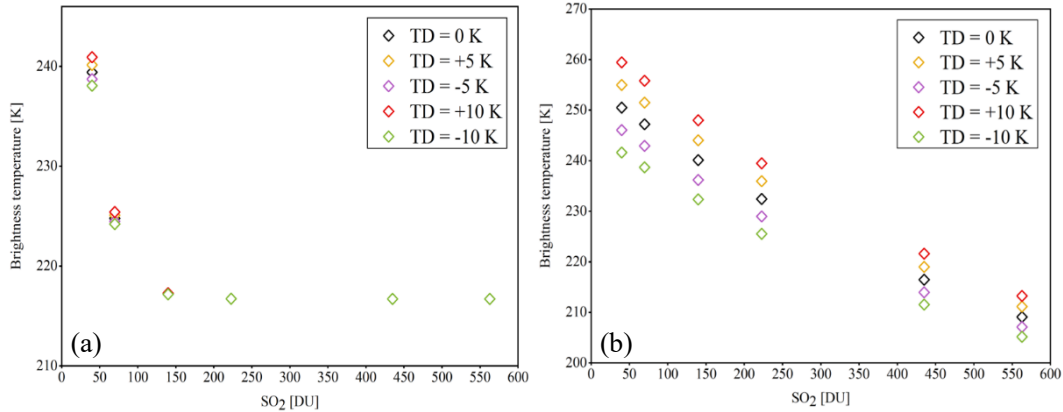


**Figure 12: Sensitivity of  $\text{SO}_2$  plume measurement at channels (a)  $1360.625$  and (b)  $1163.125 \text{ cm}^{-1}$  to surface temperature with atmospheric profiles from the US Standard Atmosphere, 1976.**

## 4.2 $\text{SO}_2$ plume sensitivity

This study assumes an atmosphere containing  $\text{SO}_2$  clouds at various altitudes and simulates the radiative transfer in a standard atmosphere with an introduced  $\text{SO}_2$  layer of varying  $\text{SO}_2$  concentration. The simulations replicate FY-3E/HIRAS-II's observations of  $\text{SO}_2$  volcanic plumes, focusing on the sensitivity of the differences in BT between central wavenumbers of  $1360.625$  and  $902.5 \text{ cm}^{-1}$  and between  $1163.125$  and  $902.5 \text{ cm}^{-1}$  to the total  $\text{SO}_2$  column in Dobson units at four plume altitudes (3, 6, 12, and 16 km). The temperature and humidity profiles for these simulations are based on the US Standard Atmosphere, 1976. Figure 13(a) shows that for  $\text{SO}_2$  plumes under varying pressure intensities, strong sensitivity is observed when  $\text{SO}_2$  content exceeds 50 DU. At 50 ~ 300 DU, the sensitivity of the  $\text{SO}_2$  plume increases with altitude. However, beyond 300 DU, the impact of altitude on sensitivity diminishes, indicating a saturation state. Thus, the  $1360.625 \text{ cm}^{-1}$  channel is prone to saturation at high  $\text{SO}_2$  concentrations. Figure 13(b) shows that for  $\text{SO}_2$  plumes below 400 DU, the  $\text{SO}_2$  Jacobian function value for the  $1163.125 \text{ cm}^{-1}$  channel is relatively low, resulting in reduced sensitivity. Conversely, above 500 DU, the channel exhibits a more pronounced response to increasing  $\text{SO}_2$  concentration and plume height.

Therefore, combining these two channels for different  $\text{SO}_2$  concentrations enables the representation of a broad range of net  $\text{SO}_2$  absorption. The brightness temperature difference between the  $1360.625$  and  $902.5 \text{ cm}^{-1}$  channels can reach up to  $\sim 70 \text{ K}$ , aligning well with previous experimental results (Ackerman et al., 2008).

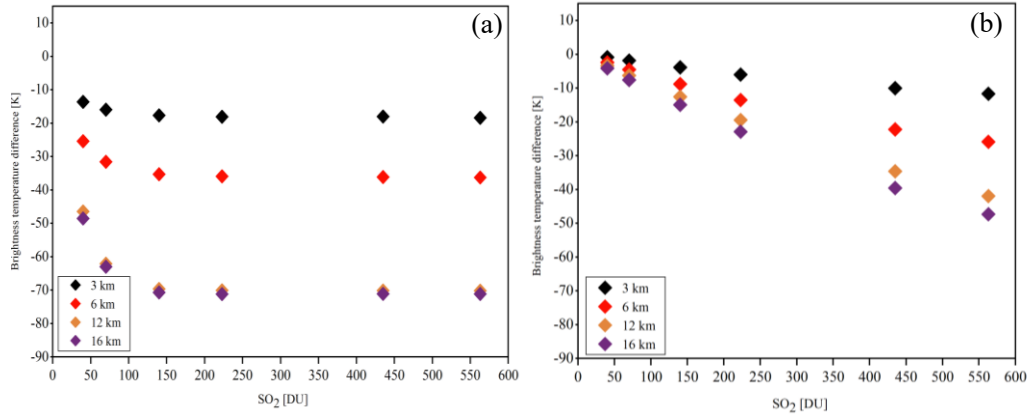


**Figure 13: Modelled FY-3E/HIRAS-II brightness temperature differences between the (a) 1360.625 and 902.5  $\text{cm}^{-1}$  channels and the (b) 1163.125 and 902.5  $\text{cm}^{-1}$  channels for assessing column  $\text{SO}_2$  content (DU) at four plume heights in atmospheric profiles derived from the US Standard Atmosphere, 1976.**

## 5 Case study

375 The channels for  $\text{SO}_2$  detection and retrieval least affected by temperature and water vapor were selected based on experimental results. To verify the accuracy of our channel selection, we compared observations of a volcanic eruption using our selected channels and normal channels.

The selected eruption was of Mount Ruang, Indonesia, the southernmost complex volcano in the Sandwich Islands. Its first recorded eruption in 1808 forced the evacuation of over 1,000 people (Galetto et al., 2024). Its violent eruption on the evening of 17 April 2024 was observed by FY-3E/HIRAS-II on 18 April. The collected data are used to explore the advantages of our  
380 selected channels.

Figure 14 depicts the differences between the following pairs of channels: 1360.625 and 902.5  $\text{cm}^{-1}$ , 1360.625 and 1429.375  $\text{cm}^{-1}$ , 1163.125 and 902.5  $\text{cm}^{-1}$ , and 1163.125 and 1887.5  $\text{cm}^{-1}$ . Comparison of the difference results of Fig. 14(a) and Fig. 14(b) indicates that the extent of the  $\text{SO}_2$  plume near the volcano's center may be mistaken for water vapor due to the background channel's inability to effectively remove the effect of water vapor from the 1360.625  $\text{cm}^{-1}$  channel. Water vapor  
385 far from the crater is prone to misclassification as  $\text{SO}_2$  gas. A comparison of the Fig. 14(c) and Fig. 14(d) sets of difference results indicates that it is challenging to separate  $\text{SO}_2$  from the atmosphere due to the smaller value of the  $\text{SO}_2$  Jacobian matrix for the 1163.125  $\text{cm}^{-1}$  channel and its lower sensitivity to  $\text{SO}_2$  information compared with the 1360.625  $\text{cm}^{-1}$  channel. In addition, the eruption increased the atmospheric temperature near the volcano, and the difference between the 1163.125 and 1887.5  $\text{cm}^{-1}$  channels cannot remove the atmospheric temperature information observed by the sensors, resulting in significant  
390 BT differences over a large area, compared to the former, the difference between the 1163.125 and 902.5  $\text{cm}^{-1}$  channels allows for a more pronounced enhancement of certain  $\text{SO}_2$  plumes, but the results were still suboptimal. Figure 14(b) shows the BT difference between the most sensitive and background channels based on the experimental selection. The chosen combination

of SO<sub>2</sub> channels filters out most of the water vapor and atmospheric temperature effects in the observation channel, resulting  
 395 in better detection of small SO<sub>2</sub> plumes.

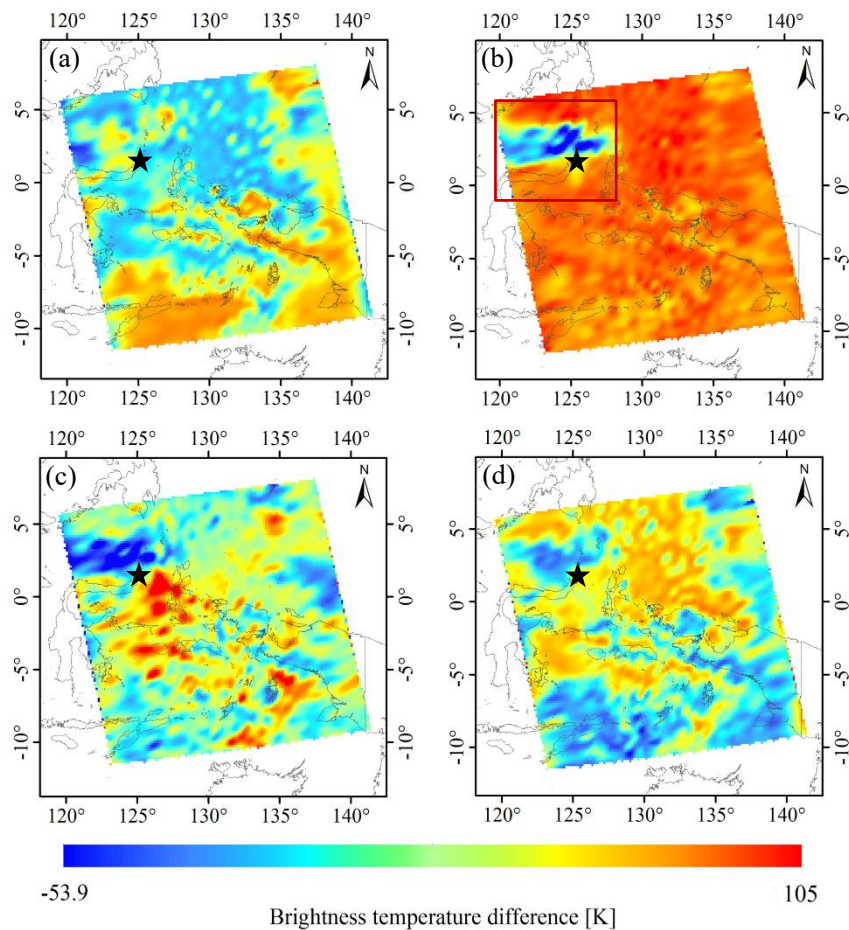


**Figure 14: FY-3E/HIRAS-II brightness temperature difference data for the region around Mount Ruang (black star in each image) at 08:55 UT on 18 April 2024 for the channels (a) 1360.625 and 902.5 cm<sup>-1</sup>, and (b) 1360.625 and 1429.375 cm<sup>-1</sup>, (c) 1163.125 and 902.5 cm<sup>-1</sup> and (d) 1163.125 and 1887.5 cm<sup>-1</sup>.**

Figure 15 compares the FY-3E/HIRAS-II BT difference data (for the area indicated by the red box in Fig. 14(b)) with corresponding observations by Sentinel-5P/TROPOMI. The area of the SO<sub>2</sub> plume’s spread and its trajectory are essentially the same for both cases. Figure 16 shows the absolute humidity data at 09:00 UT on 18 April 2024 from the ERA5 atmospheric reanalysis data at an atmospheric pressure of 400 hPa, confirming that the SO<sub>2</sub> plume observed by FY-3E/HIRAS-II in Fig. 14  
 400 is largely free of interference by water vapor.

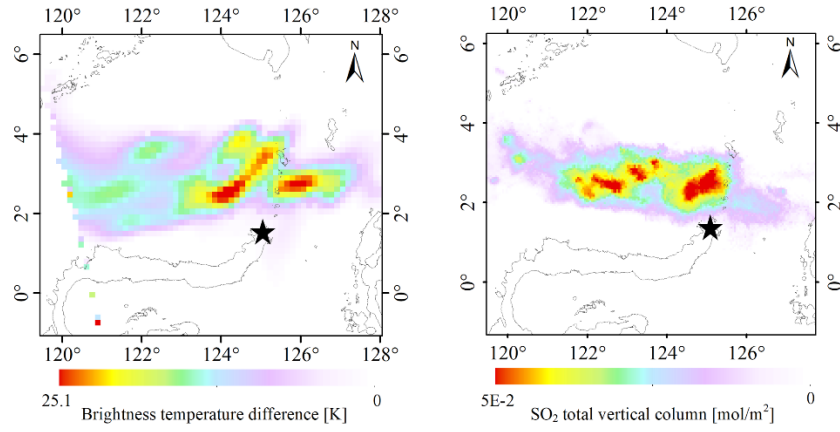


**Figure 15: Comparison of SO<sub>2</sub> around Mount Ruang (black star in each image) observed by FY3E/HIRAS-II on 18 April at 08:55 UT and Sentinel-5P/TROPOMI on 18 April at 04:07:08 UT.**

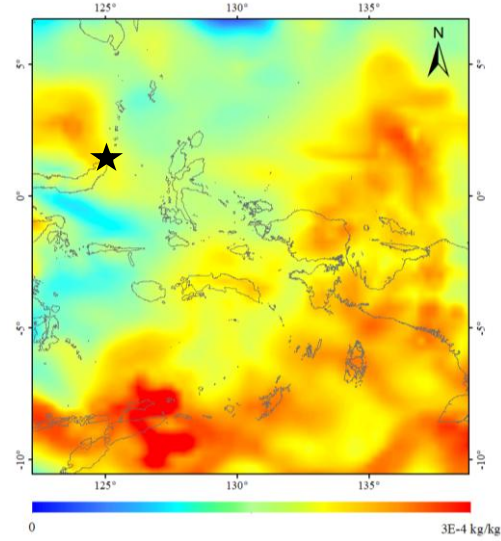


**Figure 16: Specific humidity data from ERA5 for the area around Mount Ruang (black star) at 09:00 UT on 18 April 2024 at an atmospheric pressure of 400 hPa.**

## 6 Summary and conclusion

This paper proposes a novel methodology for selecting SO<sub>2</sub> sensitive channels from FY-3E/HIRAS-II hyperspectral IR atmospheric sensors to quantitatively monitor volcanic SO<sub>2</sub>. The peak and maximum half-width of the Jacobian function of SO<sub>2</sub>, temperature and water vapor under different atmospheric conditions were cross compared to identify the optimal channels for SO<sub>2</sub> detection and retrieval. The results demonstrate that the 1360.625 cm<sup>-1</sup> channel (wavelength around 7.3 μm) is most sensitive to SO<sub>2</sub>, exhibiting a maximum peak and half width Jacobian values that conveys comprehensive SO<sub>2</sub> absorption



information. While  $1163.125\text{ cm}^{-1}$  (wavelength around  $8.6\text{ }\mu\text{m}$ ) channel has a weaker absorption to  $\text{SO}_2$  compared to  $1360.625\text{ cm}^{-1}$  channel but also contains valuable information.

Through cross-comparison of the Jacobian matrices of water vapor, temperature and  $\text{SO}_2$ , it is found that the  $1429.375\text{ cm}^{-1}$  channel (wavelength around  $7.0\text{ }\mu\text{m}$ ) can not only reflect the water vapor information to the greatest extent, but also maintain consistent variations with the atmospheric temperature and  $\text{SO}_2$ , which allows to minimize the influence of atmospheric water vapor and temperature on  $\text{SO}_2$  detection and retrieval. In the atmospheric IR window band, we identify two channels ( $902.5$  and  $901.875\text{ cm}^{-1}$ ) with the highest frequency of maximum BT under different atmospheric conditions as the land surface temperature channel to mitigate the influence of land on  $\text{SO}_2$  observations.

A sensitivity study shows that the BT difference (BTD) between the experimentally selected  $\text{SO}_2$  sensitive channel ( $1360.625\text{ cm}^{-1}$  channel) and the background channel ( $902.5\text{ cm}^{-1}$  channel) demonstrates a pronounced relationship to  $\text{SO}_2$  at  $50 \sim 300\text{ DU}$ . To address the phenomenon of saturation of the  $\text{SO}_2$  response in the  $1360.625\text{ cm}^{-1}$  channel at high concentrations, we propose to use the  $1163.125\text{ cm}^{-1}$  channel to provide auxiliary information. It is demonstrated that the  $1163.125\text{ cm}^{-1}$  channel exhibits a more significant and linear response to increasing  $\text{SO}_2$  concentration and plume height when the  $\text{SO}_2$  is above  $500\text{ DU}$ . In addition, in the lower and middle layers, a positive difference between the surface air temperature and the surface skin temperature enables the IR band to capture more  $\text{SO}_2$  information. By further analyzing the BTD between the  $1360.625\text{ cm}^{-1}$  and  $1429.375\text{ cm}^{-1}$ , the influence of water vapor and atmospheric temperature from  $1360.625\text{ cm}^{-1}$  can be effectively removed.

The main advantage of this methodology is that it comprehensively considers the interference of atmospheric temperature, humidity, and surface temperature on  $\text{SO}_2$  detection and retrieval, laying the groundwork for developing a more accurate and flexible volcanic  $\text{SO}_2$  retrieval algorithm under different atmospheric conditions. Traditional broadband multispectral satellites are seriously influenced by water vapor and atmospheric temperature in  $\text{SO}_2$  absorption region, and it is difficult to accurately separate water vapor and temperature information from  $\text{SO}_2$  sensitive channels. This methodology overcomes the above problem using satellite-based hyperspectral IR data under a Jacobian Matrix information framework. This method is able to greatly enhance the efficiency for extracting  $\text{SO}_2$  information from hyperspectral IR sounder with large number channels while maintain the accuracy. Therefore, it has great potential in both satellite-based and ground-based hyperspectral data processing for volcanic  $\text{SO}_2$  retrieval.

For future work, development of a comprehensive dataset representing a variety of volcanic ash spectral properties and atmospheric conditions for  $\text{SO}_2$  modeling, detection, and retrieval, is highly desired. Building on the dataset and the traditional line by line forward radiation transfer model, machine learning methods can help explore the nonlinear relationship between volcanic  $\text{SO}_2$  and the atmosphere/surface signals from massive forward simulated samples, as well as develop a fast and accuracy radiative transfer model for  $\text{SO}_2$  retrieval.

## CRediT authorship contribution statement

440 **Xinyu Li:** Writing – original draft, Formal analysis, Data curation, Writing – review & editing. **Lin Zhu:** Conceptualization,  
Methodology, Writing – review & editing. **Hongfu Sun:** Conceptualization, Writing – review & editing. **Jun Li:**  
Methodology, Writing – review & editing. **Ximing Lv:** Data curation. **Chengli Qi:** Resources. **Huanhuan Yan:** Resources.

## Acknowledgments

445 This research was supported by a National Natural Science Foundation of China grant Nos. 12292983 and 42271383. And  
special thanks to Professor Di di from Nanjing University of Information Science and Technology for her advice and assistance  
on Jacobian calculations.

## Declaration of competing interest

The authors declare that they have no known competing financial interests or personal relationships that could have appeared  
to influence the work reported in this paper.

## 450 Data availability

Atmosphere profile data are available via <https://doi.org/10.5281/zenodo.14174378>. TROPOMI SO<sub>2</sub> data are freely available  
via <https://doi.org/10.5270/S5P-74eidii>. The LBLRTM code are freely available via <https://doi.org/10.5281/zenodo.3837549>.  
The ERA5 specific humidity data are freely available from the Copernicus Climate Change Service (C3S) Climate Data Store  
(CDS; <https://doi.org/10.24381/cds.adbb2d47>).

455

## References

- Ackerman, S.A., Schreiner, A.J., Schmit, T.J., Woolf, H.M., Li, J.Pavolonis, M.: Using the GOES Sounder to monitor upper  
level SO<sub>2</sub> from volcanic eruptions, J. Geophys. Res., 113, D14S11, doi:<https://doi.org/10.1029/2007JD009622>, 2008.
- 460 Aires, F., Chédin, A., Scott, N.A.Rossow, W.B.: A regularized neural net approach for retrieval of atmospheric and surface  
temperatures with the IASI instrument, J. Appl. Meteorol., 41, 144-159, doi:10.1175/1520-  
0450(2002)041<0144:Arnnaf>2.0.Co;2, 2002.
- Aires, F., Pellet, V., Prigent, C.Moncet, J.-L.: Dimension reduction of satellite observations for remote sensing. Part 1: A  
comparison of compression, channel selection and bottleneck channel approaches, Q. J. R. Meteorol. Soc., 142, 2658-  
2669, doi:<https://doi.org/10.1002/qj.2855>, 2016.

- 465 Bauduin, S., Clarisse, L., Theunissen, M., George, M., Hurtmans, D., Clerbaux, C., et al.: IASI's sensitivity to near-surface carbon monoxide (CO): Theoretical analyses and retrievals on test cases, *J. Quant. Spectrosc. Radiat. Transf.*, 189, 428-440, doi:10.1016/j.jqsrt.2016.12.022, 2017.
- Carboni, E., Grainger, R.G., Mather, T.A., Pyle, D.M., Thomas, G.E., Siddans, R., et al.: The vertical distribution of volcanic SO<sub>2</sub> plumes measured by IASI. *Atmos. Chem. Phys.*, 16, 4343-4367, doi:10.5194/acp-16-4343-2016, 2016.
- 470 Carey, S.Sigurdsson, H.: The 1982 eruptions of El Chichon volcano, Mexico (2): Observations and numerical modelling of tephra-fall distribution, *Bulletin of Volcanology*, 48, 127-141, doi:10.1007/BF01046547, 1986.
- Carn, S.A., Krueger, A.J., Bluth, G.J.S., Schaefer, S.J., Krotkov, N.A., Watson, I.M., et al.: Volcanic eruption detection by the Total Ozone Mapping Spectrometer (TOMS) instruments: a 22-year record of sulphur dioxide and ash emissions, in: Oppenheimer, C., Pyle, D.M., Barclay, J. (Eds.), *Volcanic Degassing*. Geological Society of London, p. 0, 2003.
- 475 Casadevall, T.J., Rose Jr., W.I., Fuller, W.H., Hunt, W.H., Hart, M.A., Moyers, J.L., et al.: Sulfur dioxide and particles in quiescent volcanic plumes from Poás, Arenal, and Colima Volcanos, Costa Rica and Mexico, *J. Geophys. Res.*, 89, 9633-9641, doi:https://doi.org/10.1029/JD089iD06p09633, 1984.
- Chang, S., Sheng, Z., Du, H., Ge, W.Zhang, W.: A channel selection method for hyperspectral atmospheric infrared sounders based on layering, *Atmos. Meas. Tech.*, 13, 629-644, doi:10.5194/amt-13-629-2020, 2020.
- 480 Clarisse, L., Prata, F., Lacour, J.L., Hurtmans, D., Clerbaux, C.Coheur, P.F.: A correlation method for volcanic ash detection using hyperspectral infrared measurements, *Geophys. Res. Lett.*, 37, 5, doi:10.1029/2010gl044828, 2010.
- Clough, S.A.: Radiative transfer model development in support of the Atmospheric Radiation Measurement Program, United States, pp. 11-17,1994.
- Cofano, A., Cigna, F., Santamaria Amato, L., Siciliani de Cumis, M.Tapete, D.: Exploiting Sentinel-5P TROPOMI and Ground
- 485 Sensor Data for the Detection of Volcanic SO<sub>2</sub> Plumes and Activity in 2018–2021 at Stromboli, Italy, *Sensors*, 21, 6991, 2021.
- Collard, A.D.: Selection of IASI channels for use in numerical weather prediction, *Q. J. R. Meteorol. Soc.*, 133, 1977-1991, doi:10.1002/qj.178, 2007.
- Coopmann, O., Guidard, V., Fourrié, N., Josse, B.Marécal, V.: Update of Infrared Atmospheric Sounding Interferometer (IASI)
- 490 channel selection with correlated observation errors for numerical weather prediction (NWP), *Atmos. Meas. Tech.*, 13, 2659-2680, doi:10.5194/amt-13-2659-2020, 2020.
- Copernicus Sentinel-5P: TROPOMI Level 2 Sulphur Dioxide Total Column., Version 02, processed by ESA, European Space Agency [data set], <https://doi.org/10.5270/S5P-74eidii>, 2020.
- Corradini, S., Guerrieri, L., Brenot, H., Clarisse, L., Merucci, L., Pardini, F., et al.: Tropospheric Volcanic SO<sub>2</sub> Mass and Flux
- 495 Retrievals from Satellite, The Etna December 2018 Eruption. 13, 2225, doi: <https://doi.org/10.3390/rs13112225>, 2021.
- Corradini, S., Merucci, L.Prata, A.J.: Retrieval of SO<sub>2</sub> from thermal infrared satellite measurements: correction procedures for the effects of volcanic ash, *Atmos. Meas. Tech.*, 2, 177-191, doi:10.5194/amt-2-177-2009, 2009.

- Corradini, S., Merucci, L., Prata, A.J.Piscini, A.: Volcanic ash and SO<sub>2</sub> in the 2008 Kasatochi eruption: Retrievals comparison from different IR satellite sensors, *J. Geophys. Res.*, 115, doi:https://doi.org/10.1029/2009JD013634, 2010.
- 500 Corradino, C., Jouve, P., La Spina, A.Del Negro, C.: Monitoring Earth's atmosphere with Sentinel-5 TROPOMI and Artificial Intelligence: Quantifying volcanic SO<sub>2</sub> emissions. *Remote Sensing of Environment*, 315, 114463, doi:https://doi.org/10.1016/j.rse.2024.114463, 2024.
- Crevoisier, C., Chedin, A.Scott, N.A.: AIRS channel selection for CO<sub>2</sub> and other trace-gas retrievals, *Q. J. R. Meteorol. Soc.*, 129, 2719-2740, doi:10.1256/qj.02.180, 2003.
- 505 Di, D., Ai, Y.F., Li, J., Shi, W.J.Lu, N.M.: Geostationary satellite-based 6.7 μm band best water vapor information layer analysis over the Tibetan Plateau, *J. Geophys. Res.-Atmos.*, 121, 4600-4613, doi:10.1002/2016jd024867, 2016.
- Di, D., Li, J., Han, W.Yin, R.Y.: Geostationary Hyperspectral Infrared Sounder Channel Selection for Capturing Fast-Changing Atmospheric Information, *IEEE Trans. Geosci. Remote Sensing*, 60, 10, doi:10.1109/tgrs.2021.3078829, 2022.
- Doutriaux-Boucher, M.Dubuisson, P.: Detection of volcanic SO<sub>2</sub> by spaceborne infrared radiometers, *Atmospheric Research*, 510 92, 69-79, doi:https://doi.org/10.1016/j.atmosres.2008.08.009, 2009.
- Feng, G., Masek, J., Schwaller, M.Hall, F.: On the blending of the Landsat and MODIS surface reflectance: predicting daily Landsat surface reflectance, *IEEE Trans. Geosci. Remote Sensing*, 44, 2207-2218, doi:10.1109/TGRS.2006.872081, 2006.
- Fourrié, N.Rabier, F.: Cloud characteristics and channel selection for IASI radiances in meteorologically sensitive areas, *Q. J. R. Meteorol. Soc.*, 130, 1839-1856, doi:10.1256/qj.03.27, 2004.
- 515 Galetto, F., Lillo, D.L.Pritchard, M.: The use of high-resolution satellite topographic data to quantify volcanic activity at Raung volcano (Indonesia) from 2011 to 2021, *Research Square*[preprint], doi:10.21203/rs.3.rs-4364766/v1, 14 June 2024
- Gambacorta, A.Barnet, C.D.: Methodology and Information Content of the NOAA NESDIS Operational Channel Selection for the Cross-Track Infrared Sounder (CrIS), *IEEE Trans. Geosci. Remote Sensing*, 51, 3207-3216, 520 doi:10.1109/tgrs.2012.2220369, 2013.
- Gíslason, S.R., Stefánsdóttir, G., Pfeffer, M.A., Barsotti, S., Jóhannsson, T., Galeczka, I., et al.: Environmental pressure from the 2014-15 eruption of Bardarbunga volcano, Iceland, *Geochem. Perspect. Lett.*, 1, 84-92, doi:10.7185/geochemlet.1509, 2015.
- Hersbach, H., Bell, B., Berrisford, P., Biavati, G., Horányi, A., Muñoz Sabater, J., Nicolas, J., Peubey, C., Radu, R., Rozum, 525 I., Schepers, D., Simmons, A., Soci, C., Dee, D., Thépaut, J-N.: ERA5 hourly data on pressure levels from 1940 to present. Copernicus Climate Change Service (C3S) Climate Data Store (CDS) [data set], doi: 10.24381/cds.bd0915c6, 2023.
- Hersbach, H., Bell, B., Berrisford, P., Hirahara, S., Horányi, A., Muñoz-Sabater, J., et al.: The ERA5 global reanalysis, *Q J R Meteorol Soc.*, 146, 1999-2049, doi:https://doi.org/10.1002/qj.3803, 2020.
- Holasek, R.E., Self, S.Woods, A.W.: Satellite observations and interpretation of the 1991 Mount Pinatubo eruption plumes, *J. Geophys. Res.*, 101, 27635-27655, doi:https://doi.org/10.1029/96JB01179, 1996.
- 530

- Huang, J., Ma, G., Liu, G.Q., Li, J.Zhang, H.: The Evaluation of FY-3E Hyperspectral Infrared Atmospheric Sounder-II Long-Wave Temperature Sounding Channels, *Remote Sens.*, 15, 17, doi:10.3390/rs15235525, 2023.
- Inness, A., Ades, M., Balis, D., Efremenko, D., Flemming, J., Hedelt, P., et al.: Evaluating the assimilation of S5P/TROPOMI near real-time SO<sub>2</sub> columns and layer height data into the CAMS integrated forecasting system (CY47R1), based on a case study of the 2019 Raikoke eruption, *Geosci. Model Dev.*, 15, 971-994, doi:10.5194/gmd-15-971-2022, 2022.
- Jimenez-Munoz, J.C., Cristobal, J., Sobrino, J.A., Soria, G., Ninyerola, M.Pons, X.: Revision of the Single-Channel Algorithm for Land Surface Temperature Retrieval From Landsat Thermal-Infrared Data, *IEEE Trans. Geosci. Remote Sensing*, 47, 339-349, doi:10.1109/TGRS.2008.2007125, 2009.
- Krueger, A.J., Krotkov, N.A., Yang, K., Carn, S., Vicente, G.Schroeder, W.: Applications of Satellite-Based Sulfur Dioxide Monitoring, *IEEE J. Sel. Top. Appl. Earth Observ. Remote Sens.*, 2, 293-298, doi:10.1109/jstars.2009.2037334, 2009.
- Krueger, A.J., Minzner, R.A.: A mid-latitude ozone model for the 1976 U.S. Standard Atmosphere, *J. Geophys. Res.*, 81, 4477-4481, doi:https://doi.org/10.1029/JC081i024p04477, 1976.
- Kruse, F.: Predictive subpixel spatial/spectral modeling using fused HSI and MSI data, *SPIE*, doi: 10.1117/12.542631, 2004.
- Kuai, L., Natraj, V., Shia, R.-L., Miller, C.Yung, Y.L.: Channel selection using information content analysis: A case study of CO<sub>2</sub> retrieval from near infrared measurements, *Journal of Quantitative Spectroscopy and Radiative Transfer*, 111, 1296-1304, doi:https://doi.org/10.1016/j.jqsrt.2010.02.011, 2010.
- Li, J.Han, W.: A step forward toward effectively using hyperspectral IR sounding information in NWP, *Adv. Atmos. Sci.*, 34, 1263-1264, doi:10.1007/s00376-017-7167-2, 2017.
- Li, J., Menzel, W.P., Schmit, T.J.Schmetz, J.: Applications of Geostationary Hyperspectral Infrared Sounder Observations: Progress, Challenges, and Future Perspectives, *Bulletin of the American Meteorological Society*, 103, E2733-E2755, doi:https://doi.org/10.1175/BAMS-D-21-0328.1, 2022.
- Li, J.: Temperature and water vapor weighting functions from radiative transfer equation with surface emissivity and solar reflectivity. *Adv. Atmos. Sci.*, 11, 421-426, doi:10.1007/BF02658162, 1994.
- Lipton, A.E.: Satellite sounding channel optimization in the microwave spectrum, *IEEE Trans. Geosci. Remote Sensing*, 41, 761-781, doi:10.1109/tgrs.2003.810926, 2003.
- Li, S., Hu, H., Fang, C., Wang, S., Xun, S., He, B., et al.: Hyperspectral Infrared Atmospheric Sounder (HIRAS) Atmospheric Sounding System. 14, 3882, 2022.
- Milstein, A.B.Blackwell, W.J.: Neural network temperature and moisture retrieval algorithm validation for AIRS/AMSU and CrIS/ATMS, *J. Geophys. Res.-Atmos.*, 121, 1414-1430, doi:10.1002/2015jd024008, 2016.
- Noh, Y.C., Sohn, B.J., Kim, Y., Joo, S., Bell, W.Saunders, R.: A new Infrared Atmospheric Sounding Interferometer channel selection and assessment of its impact on Met Office NWP forecasts, *Adv. Atmos. Sci.*, 34, 1265-1281, doi:10.1007/s00376-017-6299-8, 2017.

- Patrick, M.R., Houghton, B.F., Anderson, K.R., Poland, M.P., Montgomery-Brown, E., Johanson, I., et al.: The cascading origin of the 2018 Klauea eruption and implications for future forecasting, *Nat. Commun.*, 11, 13, doi:10.1038/s41467-020-19190-1, 2020.
- 565 Prata, A.J.Kerkmann, J.: Simultaneous retrieval of volcanic ash and SO<sub>2</sub> using MSG-SEVIRI measurements, *Geophys. Res. Lett.*, 34, doi:https://doi.org/10.1029/2006GL028691, 2007.
- Prata, A.J., Rose, W.I., Self, S.O'Brien, D.M.: Global, Long-Term Sulphur Dioxide Measurements from TOVS Data: A New Tool for Studying Explosive Volcanism and Climate, in: *Volcanism and the Earth's Atmosphere*, pp. 75-92, 2004.
- 570 Rabier, F., Fourrié, N., Chafaï, D.Prunet, P.: Channel selection methods for Infrared Atmospheric Sounding Interferometer radiances, *Q. J. R. Meteorol. Soc.*, 128, 1011-1027, doi:10.1256/0035900021643638, 2002.
- Rose, W.I., Gu, Y., Watson, I.M., Yu, T., Blut, G.J.S., Prata, A.J., et al.: The February–March 2000 Eruption of Hekla, Iceland from a Satellite Perspective, *Volcanism and the Earth's Atmosphere*, pp. 107-132, 2004.
- Schmidt, A., Carslaw, K.S., Mann, G.W., Rap, A., Pringle, K.J., Spracklen, D.V., et al.: Importance of tropospheric volcanic aerosol for indirect radiative forcing of climate, *Atmos. Chem. Phys.*, 12, 7321-7339, doi:10.5194/acp-12-7321-2012, 575 2012.
- Seidel, F.C., Kokhanovsky, A.A.Schaepman, M.E.: Fast and simple model for atmospheric radiative transfer, *Atmos. Meas. Tech.*, 3, 1129-1141, doi:10.5194/amt-3-1129-2010, 2010.
- Senf, F.Deneke, H.: Uncertainties in synthetic Meteosat SEVIRI infrared brightness temperatures in the presence of cirrus 580 clouds and implications for evaluation of cloud microphysics, *Atmospheric Research*, 183, 113-129, doi:https://doi.org/10.1016/j.atmosres.2016.08.012, 2017.
- Shibata, T.Kinoshita, T.: Volcanic aerosol layer formed in the tropical upper troposphere by the eruption of Mt. Merapi, Java, in November 2010 observed by the spaceborne lidar CALIOP, *Atmospheric Research*, 168, doi:10.1016/j.atmosres.2015.09.002, 2015.
- 585 Taylor, I.A., Preston, J., Carboni, E., Mather, T.A., Grainger, R.G., Theys, N., et al.: Exploring the Utility of IASI for Monitoring Volcanic SO<sub>2</sub> Emissions, *Journal of Geophysical Research: Atmospheres*, 123, 5588-5606, doi:https://doi.org/10.1002/2017JD027109, 2018.
- Theys, N., De Smedt, I., Yu, H., Danckaert, T., van Gent, J., Hörmann, C., et al.: Sulfur dioxide retrievals from TROPOMI onboard Sentinel-5 Precursor: algorithm theoretical basis. *Atmos. Meas. Tech.*, 10, 119-153, doi:10.5194/amt-10-119-590 2017, 2017.
- Theys, N., Hedelt, P., De Smedt, I., Lerot, C., Yu, H., Vlietinck, J., et al.: Global monitoring of volcanic SO<sub>2</sub> degassing with unprecedented resolution from TROPOMI onboard Sentinel-5 Precursor. *Scientific Reports*, 9, 2643, doi:10.1038/s41598-019-39279-y, 2019.
- Thomas, H.E.Watson, I.M.: Observations of volcanic emissions from space: current and future perspectives. *Natural Hazards*, 54, 323-354, doi:10.1007/s11069-009-9471-3, 2010.
- 595

- Tournigand, P.Y., Cigala, V., Lasota, E., Hammouti, M., Clarisse, L., Brenot, H., et al.: A multi-sensor satellite-based archive of the largest SO<sub>2</sub> volcanic eruptions since 2006, *Earth Syst. Sci. Data*, 12, 3139-3159, doi:10.5194/essd-12-3139-2020, 2020.
- Tsuchiya, K.J.A.i.S.R.: Selection of sensors and spectral bands of marine observation satellite (MOS)—1, *Advances in Space Research*, 3, 257-261, doi:10.1016/0273-1177(83)90128-X, 1983.
- van Geffen, J., Boersma, K.F., Eskes, H., Sneep, M., ter Linden, M., Zara, M., et al.: S5P TROPOMI NO<sub>2</sub> slant column retrieval: method, stability, uncertainties and comparisons with OMI. *Atmos. Meas. Tech.*, 13, 1315-1335, doi:10.5194/amt-13-1315-2020, 2020.
- Ventress, L.Dudhia, A.: Improving the selection of IASI channels for use in numerical weather prediction, *Q. J. R. Meteorol. Soc.*, 140, 2111-2118, doi:10.1002/qj.2280, 2014.
- Watson, I.M., Realmuto, V.J., Rose, W.I., Prata, A.J., Bluth, G.J.S., Gu, Y., et al.: Thermal infrared remote sensing of volcanic emissions using the moderate resolution imaging spectroradiometer, *Journal of Volcanology and Geothermal Research*, 135, 75-89, doi:https://doi.org/10.1016/j.jvolgeores.2003.12.017, 2004.
- Xie, M., Gu, M., Hu, Y., Huang, P., Zhang, C., Yang, T., et al.: A Study on the Retrieval of Ozone Profiles Using FY-3D/HIRAS Infrared Hyperspectral Data, *Remote Sens.*, 15, 1009, doi: https://doi.org/10.3390/rs15041009, 2023.
- Yang, F.Schlesinger, M.E.: On the surface and atmospheric temperature changes following the 1991 Pinatubo volcanic eruption: A GCM study, *J. Geophys. Res.*, 107, ACL 8-1-ACL 8-14, doi:https://doi.org/10.1029/2001JD000373, 2002.
- Zhang, P., Hu, X., Lu, Q., Zhu, A., Lin, M., Sun, L., et al.: FY-3E: The First Operational Meteorological Satellite Mission in an Early Morning Orbit, *Adv. Atmos. Sci.*, 39, 1-8, doi:10.1007/s00376-021-1304-7, 2022.